Tunable mechanical behavior of auxetic cementitious cellular composites (CCCs) Experiments and simulations

Xu, Yading; Schlangen, Erik; Luković, Mladena; Šavija, Branko

DOI
10.1016/j.conbuildmat.2020.121388

Publication date
2020

Document Version
Final published version

Published in
Construction and Building Materials

Construction and Building Materials 266 (2021) 121388

Contents lists available at ScienceDirect

Construction and Building Materials

journal homepage: www.elsevier.com/locate/conbuildmat

Tunable mechanical behavior of auxetic cementitious cellular composites (CCCs): Experiments and simulations

Yading Xu *, Erik Schlangen, Mladena Luković, Branko Šavija

Faculty of Civil Engineering and Geosciences, Delft University of Technology, 2628 CN, Delft, the Netherlands

HIGHLIGHTS

- Cracking-initiated rotation is found as the deformation mechanism of auxetic cementitious cellular composites (CCCs).
- Compressive behavior of CCCs is found to be crucially influenced by its geometry features.
- Re-entrant shape confine zones are discovered for auxetic CCCs under restrained boundary condition.

ARTICLE INFO

Article history:
Received 6 June 2020
Received in revised form 14 October 2020
Accepted 18 October 2020
Available online 3 November 2020

Keywords:
Cementitious cellular materials
Negative Poisson's ratio
Numerical simulation
Boundary conditions

ABSTRACT

This research presents an investigation of the compressive behavior of auxetic cementitious cellular composites (CCCs) using a combination of experiments and finite element (FE) simulations. Typical auxetic centrosymmetric geometry was used as unit cells for the cellular structure and fiber reinforced cementitious mortar were used as constituent material. By varying the cellular geometry, three CCCs (P0, P25 and P50) were prepared then experimentally and numerically tested under uniaxial compression with different boundary conditions. Good agreement can be found between experimental and FE simulated results: Only CCCs with chiral section (P25 and P50) exhibited auxetic behavior and a typical compressive stress–strain response with two peaks was found; Under restrained boundary condition, different from the cone confinement zone observed in bulk cementitious materials, re-entrant confinement zone was found in the auxetic CCCs. More importantly, a cracking initiated section rotation mechanism is identified for the CCCs' auxetic behavior which is distinct from the elastic instability mechanism of polymeric auxetic materials with the same cellular structure. In terms of density, energy dissipation ability and Poisson's ratio, the auxetic CCCs shows excellent properties making them promising in various civil engineering applications.

1. Introduction

The term "auxetic", first coined by Evans [1] in 1990 s, refers to materials exhibiting negative Poisson's ratio (NPR). The value of Poisson's ratio is defined as the negative of the ratio of transverse strain to the corresponding axial strain resulting from an axial stress. Contrary to conventional materials which show a positive Poisson's ratio, auxetic materials contract laterally when compressed vertically or expand laterally when elongated vertically [2,3]. Auxetic materials have been an extremely hot topic over the past few years, and auxetic behavior has been achieved by different types of materials such as metals [4–6], ceramics [7,8], polymers [9–13], and composites [14,15].

Auxetic behavior is usually achieved by introducing special cellular structures [13,16]. By programming the cellular structure [13,17] or modifying the constituent materials [12], mechanical properties of the auxetic materials can be rationally designed. Compared to conventional continuum solids, auxetic materials possess outstanding advantages regarding their mechanical properties in several aspects: on one hand, the cellular structure constructed by periodic unit cells affords them considerably lower weight [18–20] comparing to continuum solids. This not only reduces materials usage but expands their application occasions where weight is a crucial factor, for instance in aircrafts [21,22] and protection fabrics [23–25]. On the other hand, the unique deformation behavior, i.e. NPR of auxetic materials enables them superior mechanical properties such as high shear resistance, high indentation resistance, high energy absorption, and high damping capability [26]. These mechanical excellences make auxetic materials rather promising in many infrastructure engineering

* Corresponding author.
E-mail address: y.xu-5@tudelft.nl (Y. Xu).

https://doi.org/10.1016/j.conbuildmat.2020.121388
0950-0618/

applications such as barriers for impact resistance, offshore breakwaters, dampers for vibration mitigation caused by vehicles or, even in extreme conditions, earthquakes. Compared to other construction materials, such as steel and timbers, cementitious materials, which are the most widely used construction materials, are particularly suitable for these applications because of their capability of obtaining outstanding mechanical properties and durability at relatively low cost. In addition, processing of cementitious materials is quite easy and robust: normally a flowable cementitious mix is directly casted into molds, which ensures the feasibility of adopting cellular structures. Recently, cementitious cellular composites (CCCs) with auxetic behavior have been reported [27,28] by adopting a centrosymmetric chiral (meaning that each unit cell is symmetric however consisted by chiral parts at a centrosymmetric configuration) cellular structure which enables the auxetic CCCs to exhibit excellent deformability and energy dissipation capability.

The adopted centrosymmetric chiral structures by [27,28] are usually identified as "elastic-instability" structures in which the auxetic mechanism is attributed to elastic buckling. In this sense, materials with high deformability, such as polymeric materials, are often used for this type of structures to achieve auxetic behavior. For those commonly used polymers, varying geometrical features of the centrosymmetric chiral structure considerably affects the mechanical properties of the constituted auxetic materials in a large range regarding the stiffness [4,10,29], strength [4,10,29] and deformation localization [30,31] which is the mechanism of NPR behavior. For cementitious materials, similar influence can be identified from the preliminary study by [28]. However, the basic NPR mechanism in CCC's has not yet been fully understood. For a same type of cellular structure, cementitious materials with low deformability and prone to cracking still achieved NPR in [24,25], which indicates an NPR mechanism related to cracking. Usually, boundary restraint condition is believed to significantly impact cracking behavior [32,33] of cementitious materials. For bulk cementitious materials, because of their positive Poisson's ratio (0.15 to 0.22 [34–37]), the lateral expansion is restrained when vertically compressed by the friction between the specimen and the loading plates. As a result, the compressive behavior such as strength and cracking pattern is different from unrestrained condition. However, for auxetic cementitious materials, because of the NPR lateral contraction instead of expansion is restrained by the loading plates and the frictional restraining force direction is inverted. In this sense, the influence of boundary restraint on the compressive behavior of the auxetic cementitious materials may be rather different.

Programming cellular structures of the auxetic cementitious materials makes a new material developing strategy which, however, requires a rational understanding on the NPR mechanism, the impact of geometrical features and boundary conditions on the mechanical behavior of auxetic materials. This work presents an in-depth investigation of mechanical behavior of auxetic cementitious cellular composites (CCCs) with tuned geometrical features under different boundary conditions. CCCs with a centrosymmetric chiral structure were prepared with the aid of 3D printing technology. By varying geometrical parameters of the unit cell, three types of CCCs were designed, produced and submitted to uniaxial compression under various levels of boundary restraint. In addition to the experiments, finite element numerical models were adopted, calibrated and used to simulate the compression process of the CCCs. With regard to the NPR mechanism, the influence of geometrical features and boundary conditions on the mechanical properties of the auxetic CCCs, analyses coupling experiment and numerical simulation were performed.

2. Materials and methods

2.1. Cellular geometry design parameters

Three types of geometry were used in this study. A single unit cell of the cementitious cellular composites (CCCs) is shown in Fig. 1. Geometry parameters are listed in Table 1. The designed CCCs consist of duplicate unit cells: an example of the designed CCCs was shown in Fig. 2. The pattern deformation factor of each group is defined as the increased length percentage of the major axis comparing to P0.

2.2. Casting and curing

The same method described in [28] was adopted to prepare CCCs specimens: the designed cellular structures were 3D printed by a commercial fused deposition modelling (FDM) based 3D printer Ultimaker 2 + using acrylonitrile butadiene styrene (ABS) material. The printed structures were glued inside cubic boxes as negative molds. Then, a two-component silicone rubber (Poly-Sil PS 8510) was mixed together and casted into the negative molds. After 2 h, the hardened silicone rubber was taken out of the cubic box and further used as mold for cementitious material casing afterwards. Note that, depending on the printing quality, the actual dimension of the molds may vary within 0.8 mm from the design parameters as 0.8 mm nozzle was used.

A fine-grained fiber reinforced mortar was used as constituent material for the CCCs. CEM I 42.5 N and fly ash were used as binder, PVA fiber was used as reinforcement by 2% of volume. The PVA fiber was produced by Changzhou TianYi Engineering Fiber. Physical and mechanical parameters of the PVA fibers are shown in Table 2. To obtain better fiber distribution, methylcellulose powder produced by Shanghai Ying Jia Industrial Development Co. Ltd. was used as viscosity modifying agent (VA). Mix proportion is listed in Table 3.

Dry components (CEM I 42.5, fly ash, sand, VA) were weighed and mixed for four minutes using a Hobart machine. Then water and superplasticizer were weighted and added to the dry components followed by 2 min mixing. Afterwards fibers were added into the mixed materials and mixed for another 2 min. The mixed fresh grout was casted into the silicone molds, steel molds (100 mm × 100 mm × 100 mm) and Styrofoam (180 mm × 180 mm × 8 mm) molds respectively. All casted materials were vibrated for 40 s and covered by plastic films to prevent evaporation. After curing under room temperature for 1 day the specimens were demolded and cured in the curing chamber (20℃, 96%RH) until 28 days age. Plate specimens (shown in Fig. 3a) demolded from Styrofoam molds were cut into bars (100 mm × 30 mm × 8 mm, shown in Fig. 3b). Cube specimens (Fig. 3c) demolded from steel molds were cut into small cubes (20 mm × 20 mm × 20 mm, Fig. 3d).

2.3. Mechanical tests

All specimens were taken out of the curing chamber an hour before testing. In order to calibrate the numerical model (ABAQUS/Explicit), six bar specimens were tested under uniaxial tension, and six cubic specimens were tested under uniaxial compression. The results of these tests are presented in section 3, where the numerical modelling is discussed.

The CCCs were tested under uniaxial compression, four duplicate specimens were tested for each design. One surface of the specimens was painted white and sprayed with red dots in order to perform DIC (digital image correlation). Images were acquired

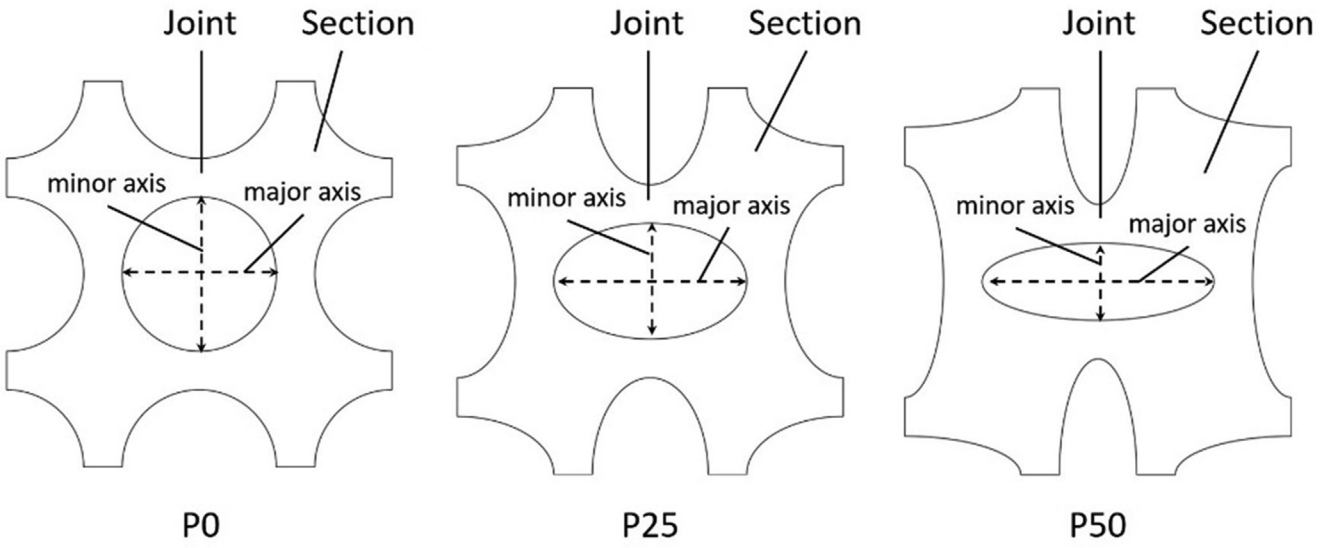

Fig. 1. Design parameters of cementitious cellular composites.

Table 1
Specimen groups with different design parameters and boundary conditions.

Specimen groups	Major axis (mm)	Minor axis (mm)	Ellipse area (mm^2)	Pattern deformation factor	Specimen Volume (cm^3)	Relative density	Boundary condition
P0*	8	8	50.24	0	63.66	49.7%	Low friction
P25*	10	6	47.10	25	67.68	52.8%	Low friction
P50	12	4	37.68	50	79.75	62.3%	Low friction
P25SG	10	6	47.10	25	67.68	52.8%	Single side glued
P25DG	10	6	47.10	25	67.68	52.8%	Double side glued

*Design parameters of P0 and P25 are adopted from [27,28].

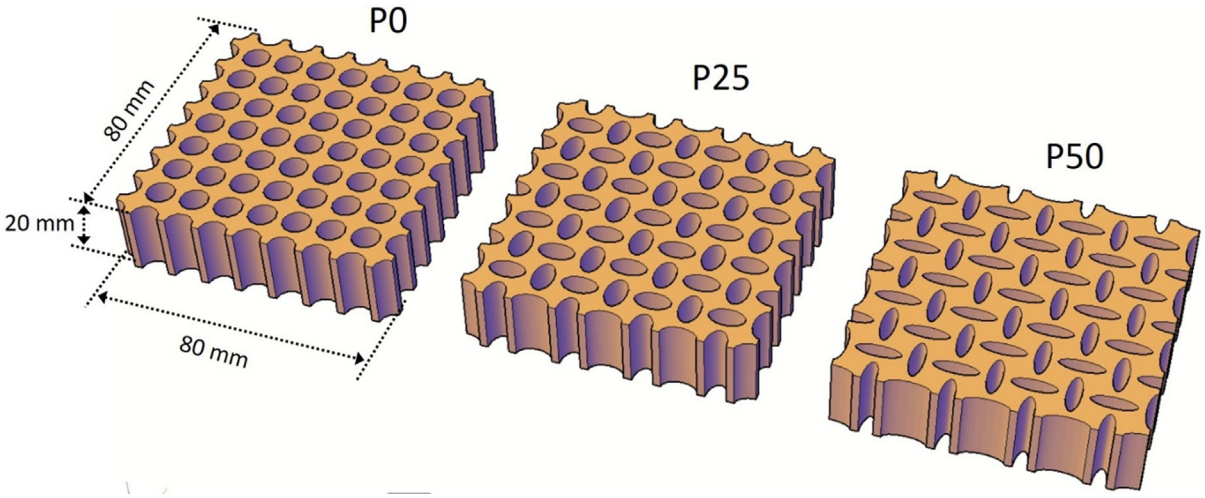

Fig. 2. Designed CCCs specimens.

Table 2
Properties of PVA fibers used in the cementitious matrix.

Diameter	Length	Tensile Strength	Young's modulus	Density
15 μm	6 mm	1.6 GPa	34 GPa	1.28 g/cm^3

every second during testing by a camera which was placed in front of the specimen. By adopting DIC analysis, local translational shift of the sprayed dots on the specimen was computed. Thus, the displacement of the sprayed dots was obtained and full-filed deformation of the specimen was able to be obtained during the entire compression process. In order to calculate the Poisson's ratio, the

Table 3
Mix proportion of constituent materials (kg/m^3).

CEM I 42.5 N	Fly ash	Sand (0.125 to 0.250 mm)	Water	Superplasticizer (Glenium 51)	VA	PVA Fiber
471	556	385	428	0.86	0.3	25.6

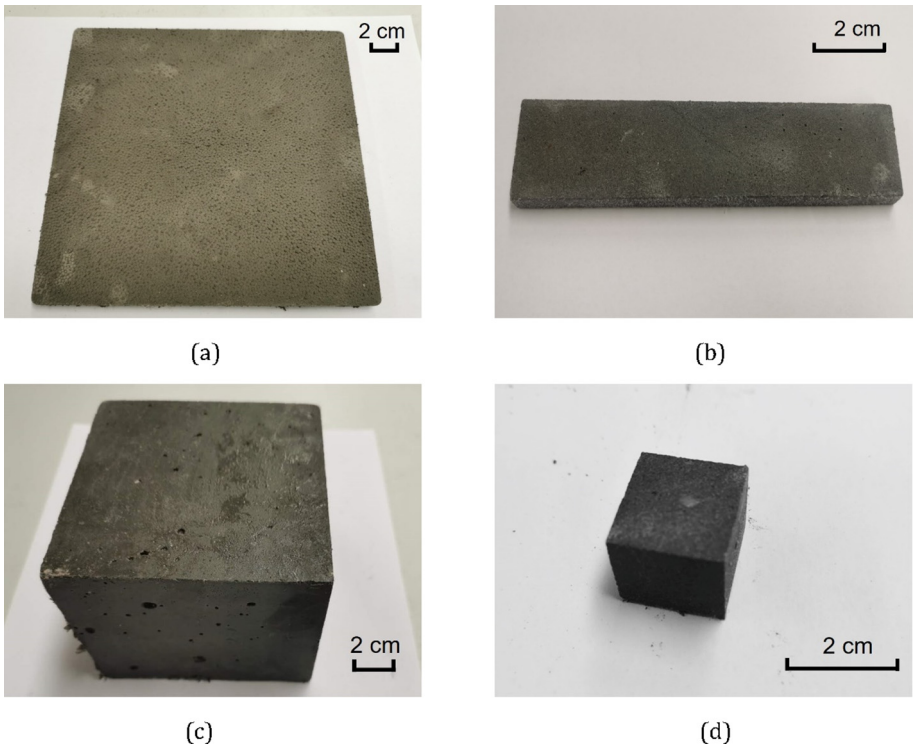

Fig. 3. Specimens before cutting and after cutting, a) plate specimen; b) bar sepcimen; c) 100 mm cube; d) 20 mm cube.

middle height and top side of the specimen was chosen as the references for specimen horizontal deformation and vertical deformation, respectively. The Poisson's ratio is calculated as the ratio of the horizontal deformation to the vertical deformation.

All mechanical tests were done using a hydraulic press (INSTRON 8872). The loading rate for all tests were fixed at 0.01 mm/s. Load and displacement were measured and recorded during the tests. The results of the experiments on the CCC specimens are discussed in section 4.

3. Numerical modelling

In order to provide further understanding of the compressive behavior and NPR mechanism of the CCCs. Numerical models were adopted to simulate the compression process of the CCCs. The simulations were performed by a commercial numerical package (ABAQUS/Explicit). Geometric nonlinearity (Nlgeom) was used and concrete damage plasticity model (CDPM) which is commonly used for simulating fiber reinforced cementitious materials [38–40] in ABAQUS was used as material model for the constituent material in this study. According to ABAQUS guide documents, the constitutive equation of CDPM can be described as follows:

$$\sigma = (1-d)E_0\left(\varepsilon - \varepsilon^{pl}\right) \tag{1}$$

Where is σ Cauchy stress; ε and ε^{pl} are total strain and equivalent plastic strain respectively; E_0 is initial elastic modulus. In the presence of modulus degradation, d is damage variable and can be defined from 0 to 1. In our study, stiffness degradation in not considered.

The yield criterion beyond which the plastic strain initiates of CDPM is given as:

$$F = \frac{1}{1-\alpha}\left(\overline{q} - 3\alpha\overline{p} + \beta\left(\varepsilon^{pl}\right)\left\langle\widehat{\overline{\sigma}}_{max}\right\rangle - \gamma\left\langle-\widehat{\overline{\sigma}}_{max}\right\rangle\right) - \widehat{\overline{\sigma}}_c\left(\varepsilon_c^{pl}\right) \tag{2}$$

With

$$\alpha = \frac{(\sigma_{b0}/\sigma_{c0}) - 1}{2(\sigma_{b0}/\sigma_{c0}) - 1} \tag{3}$$

$$\beta = \frac{\overline{\sigma_c}\left(\varepsilon_c^{pl}\right)}{\overline{\sigma_t}\left(\varepsilon_t^{pl}\right) - 1}(1-\alpha) - (1+\alpha) \tag{4}$$

$$\gamma = \frac{3(1-K_c)}{2K_c - 1} \tag{5}$$

Where, $\widehat{\overline{\sigma}}_{max}$ is maximum principal effective stress; σ_{b0}/σ_{c0} is the ratio of initial equi-biaxial compressive yield stress to initial uniaxial compressive yield stress which has an ABAQUS default value of 1.16 and adopted as input normally. K_c describes the tensile meridian second stress invariant to that on compressive meridian for a given invariant p, $0.5 < K_c \leq 1$ must be satisfied and as an ABAQUS default value $K_c = 0.667$ is also adopted by many researches.

Non-associated potential plastic flow is assumed for CDPM and the flow potential G is described as:

$$G = \sqrt{(\epsilon\sigma_{t0}\tan\psi)^2 + \overline{q}^2} - \overline{p}\tan\psi \tag{6}$$

Where ψ is the dilation angle, σ_{t0} is the uniaxial tensile failure strength, ϵ is the eccentricity which determines the rate at which the function approaches the asymptote. $\epsilon = 0.1$ is adopted as a default value.

According to CDPM, uniaxial compression and tension response are characterized by plasticity, the evolution of the failure is controlled by compressive plastic strain ε_c^{pl} and tensile plastic strain ε_t^{pl}, respectively. These two variables can be determined by material uniaxial loading behavior as shown in Fig. 4. Under compression, the failure stress (σ_{c0}) corresponds to onset of microcracking of the cementitious material after elastic stage. Under tension, the failure stress (σ_{tu}) corresponds to the ultimate tensile strength. The compressive inelastic strain (ε^{in}) and tensile crack strain (ε^{ck}) is defined as the total strain minus the elastic strain corresponding to the undamaged material, respectively. In this study, E-modulus degradation is not defined, in this sense compressive plastic strain $\varepsilon_c^{pl} = \varepsilon^{in}$ and tensile plastic strain $\varepsilon_t^{pl} = \varepsilon^{in}$.

3.1. Model calibration

Prior to simulating the uniaxial compression behavior of the CCCs, the models were calibrated to obtain proper material input parameters. By fitting uniaxial compression tests on the cubic specimens and uniaxial tension tests on the bar specimens, compressive behavior parameters and tensile behavior parameters of the constituent material can be obtained as model inputs. Balancing model precision and computing cost, two-dimensional plane stress elements with a mesh size of 0.5 mm were chosen and kept constant for all numerical simulations in this study. As described previously, in the CDPM inelastic and cracking strains are used to model the material damage in compression and tension, respectively. Therefore, besides the elastic modulus, density (shown in Table 4) and plasticity parameters (adopted from literature [40], where a rather similar mix was used), inelastic regime (compression) and post peak cracking regime (tension) of the stress–strain response need to be specified to simulate the damage process. Fig. 5a shows the stress–strain curves (blue dashed lines) of the cubic specimens obtained from uniaxial compression experiments. As the constituent material is fiber reinforced, rather ductile

Table 4
Material input parameters.

Material input parameters	Value
Density (kg/m^3)	1870
Elastic Modulus (MPa)	8230
Poisson's Ratio	0.2
Dilation Angle(ψ,°)	35
Eccentricity (ϵ)	0.1
σ_{b0}/σ_{c0}	1.16
K_c	0.667
Viscosity parameter	0.001

compressive damage behavior can be identified from the experimental results: stress increased as compression initiated and kept increasing until compressive strength was reached. Afterwards, the stress started to drop slowly which is normally described as a softening branch [33,41]. Comparing to the typical quasi-brittle damage of unreinforced cementitious material [33,41], the softening branch of fiber reinforced cementitious material is considerably longer as the fibers significantly increase the material ductility. In the stress–strain curves (see Fig. 5a), a long plateau stage was observed from experiments. Several points were chosen by averaging strain and stress values based on the experiment curves (plotted as black dots connected by green line in Fig. 5a) and then used as material inputs for simulation (listed in Table 5 and Table 6, note that in ABAQUS, tension input strain need to be converted to displacement accordingly), the material compressive curve is plotted as green line in Fig. 5a). A numerical compression test was performed using the constitutive curve. The simulated result is also plotted Fig. 5a, marked as "Calibration" (red line). The simulated compression curve shows good agreement with experiment curves, indicating that the material compressive parameters are calibrated.

A similar calibration approach was also applied for tension model input parameters. The comparison of model input curves and experimental curves are shown in Fig. 5b. After the first crack (witnessed by a sharp drop of the stress-inelastic strain curve), the specimen did not fail completely, owning the so called "slip hardening" behavior [42–45]. Slip hardening is often witnessed in PVA fiber reinforced cementitious materials. PVA fibers are flexible and

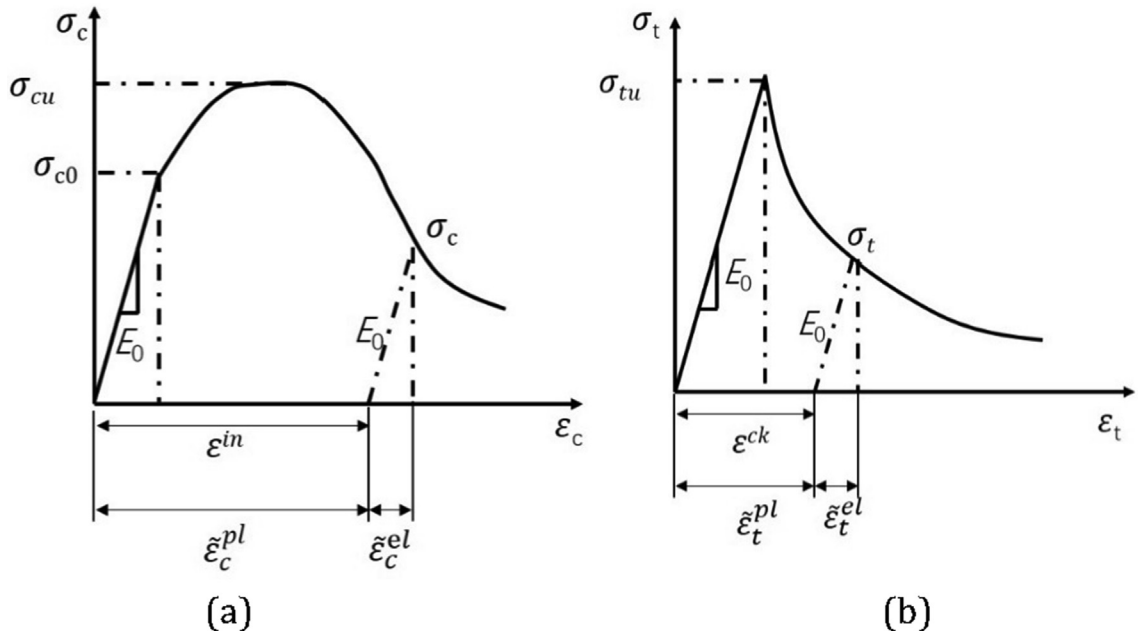

Fig. 4. Definition of uniaxial a) compressive and b) tensile behavior for CDPM.

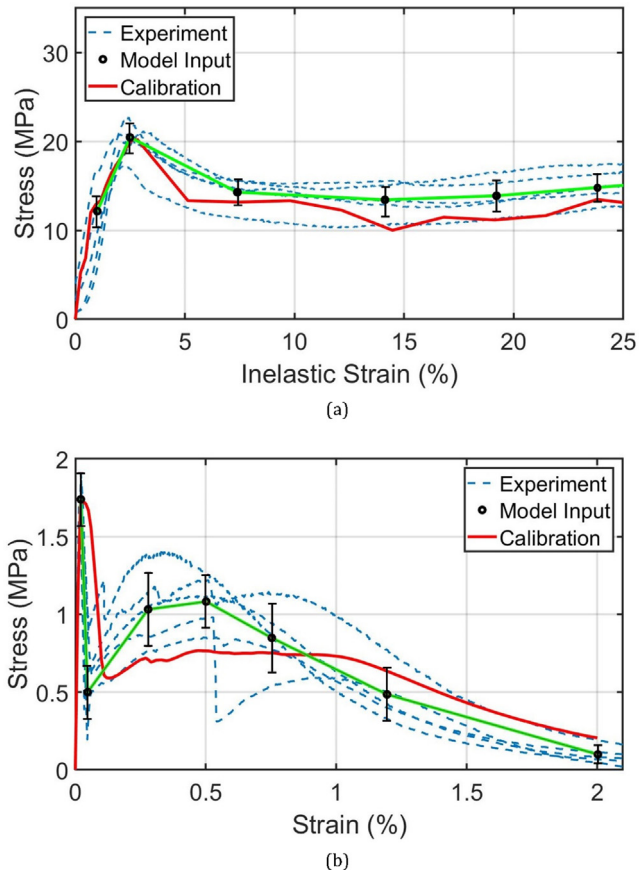

Fig. 5. Comparison of experimental, model input and calibration curves in (a) uniaxial compression and (b) uniaxial tension, standard deviations of the input points are indicated in both figures.

Table 5
Compressive behavior parameters.

Yield stress (MPa)	Inelastic strain (%)
12.156	0
20.532	1.49
15.06	6.39
14.076	13.13
14.46	18.21
14.472	24.56

Table 6
Tensile behavior parameters.

Yield stress (MPa)	Cracking strain (%)
1.74	0
0.5	0.05
1.08	0.26
1.08	0.48
0.85	0.73
0.49	1.17
0.1	2

less hard comparing to its embedding cementitious matrix. When crack opening increase, these PVA fibers are slowly pulled out from the matrix and polymeric branches are peeled off from the PVA fiber by the hard matrix. As a result, a jamming effect generates between the PVA fiber and the matrix which resists fiber pullout and leads to an increasing load after cracking. Owing to this slip hardening behavior, the load still increased again until a second peak was reached. The constituent material does not show strain hardening behavior and as a result only one crack was witnessed. In this study, as the tension specimens were meshed homogenously (no mesh heterogeneity was introduced comparing to what discrete models [46–50] usually do), inelastic deformation will be easily localized at where it initiates. As a result, the slip-hardening behavior will be rather difficult to be captured by simulation thus the simulated second peak is slightly lower than the experiment (Fig. 5b red line). In any case, the simulated curve still shows good agreement with experiment, in this case the tension model input parameters are also well calibrated regarding the good agreement between simulation and experiment.

Normally, for CDPM compression and tension damage parameters can be assigned which is used to capture E-modulus degradation during unloading process. However, in this study as unloading process was not included in the experiment these damage parameters were not specifically assigned. Therefore, according to the CDPM constitutive law, compressive inelastic strain and tensile cracking strain are assumed to be equal to plastic strain which indicates damage, as described previously.

3.2. Simulation of compressive tests on CCCs

ABAQUS/Explicit was used to simulate the compression process of the CCCs. As shown in Fig. 6, in order to simulate the real experimental condition of the compression tests, in the numerical model external load was not directly applied on the specimen, instead, two loading plates (160 mm in length and 5 mm in height) were added as rigid body parts and placed at the top and the bottom of the specimen. Vertical displacement was applied downwards on the top plate while the bottom plate was fixed.

In addition, according to the experimental conditions (listed in Table 1), the specimen P25 was tested under three types of boundary restraint conditions: low friction boundary condition which simulates the unrestrained compression test (P25), single side confined boundary condition which simulates the single side glued compression test (P25SG) and both sides confined boundary condition which simulates the double side glued compression test (P25DG) test. Correspondingly, three types of contact rules were applied between the specimen and the steel plates in the simulations, respectively. For low friction boundary conditions, although plastic films were applied between the specimen and loading plates, slight friction still occurred during testing. Under ideal frictionless condition (friction coefficient is 0), the specimen would move horizontally in the simulation when compressed which however, doesn't match practical experiment conditions. So, by a trial and error method, the friction coefficient is increased from 0 until the compressed specimens don't move horizontally meanwhile the simulated deformation process of the unit cells in contact with the plates shows good agreement with experiment. Therefore, a low friction coefficient 0.105 was assumed and used to simulate the slight friction between the specimen and loading plates. Comparatively, for single side glued condition, glued elements at the specimen top were completely tied with the loading plate while the bottom side is the same with low friction boundary condition; for double side glued condition, glued elements at both sides of the specimen were completely tied with the top and bottom loading plates, respectively. Similar to previous approach, the friction coefficient between the constituent materials is decreased from 1 until the deformation pattern matches experiment, which consequently also ensures the stress–strain response in agreement with experiment. A friction coefficient 0.95 is assumed as the self-contact parameter between the constituent material elements.

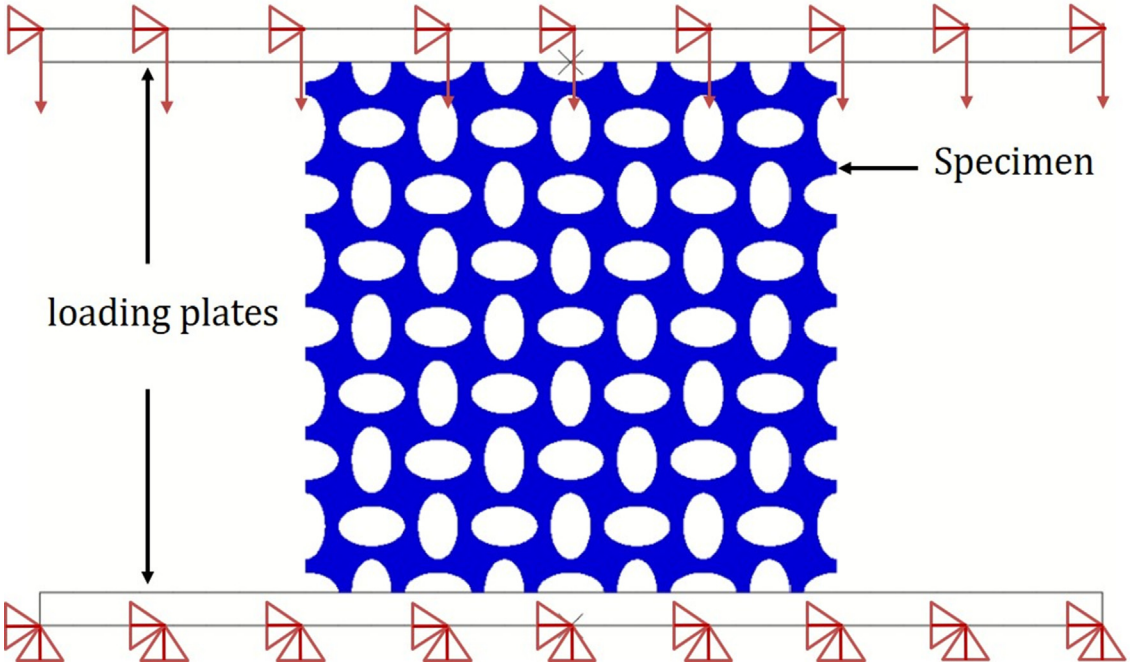

Fig. 6. Simulation set-up for compression of the CCCs.

4. Results and discussion

4.1. Influence of geometrical features

Fig. 7 and Fig. 9 show the stress–strain curves and compression process (until 40% strain) obtained from experiments and numerical simulations of the CCC specimens. Note that as the CDPM is used in the simulation, cracks are simulated by plastic deformation. Therefore, highly deformed locations in Fig. 7 and Fig. 9 show high plastic strain which correspond to the cracks observed in experiments. In general, owing to the difference in geometrical features, P0, P25 and P50 behave significantly different during the compression process. With regard to the entire compressive behavior, for all tested three different geometries, a very good agreement was found between experimental results and numerical simulations.

The compressive behavior of P0 resembles the compressive damage process of conventional fiber reinforced cementitious materials [39,51]: a single peak can be found during the entire compression process. In the pre-peak regime, an ascending branch can be found in the stress–strain curves (Fig. 7a), specimen deformed elastically as soon as external load was applied. When the peak load was reached, cracks started to appear and propagate through the cellular structure. It can be seen from both experiment and simulation in Fig. 7b, cracks (high strain area) propagated through the cellular structure by connecting hollow parts of the specimen forming shear crack planes which is commonly found in the compressive failure process of conventional cementitious materials [33]. At the macroscale, although the diagonal fracture plane looks very similar to shear bands caused by plastic slip (which is the failure mode of ductile materials), the microscopic mechanism for the CCCs is very different. Indeed, the PVA fiber reinforced material shows some ductility after the peak load (see tensile stress–strain curve in Fig. 5b), but this is caused by the fiber bridging after cracking. So, the microscopic mechanism of the failure of CCCs is still brittle cracking. Cementitious materials are very heterogenous, and their compressive failure is a process of tensile microcracking (Mode I fracture at microscale) inclined to the shear direction [52]. Depending on the boundary conditions, inclination angle of the shear fracture plane varies: under frictionless condition, an inclination around 21 degrees has been observed [33]. For cellular materials, the fracture plane must follow the configuration of the cellular structure/elements, as voids cannot transfer stresses. A similar phenomenon is commonly witnessed in discrete element fracture modeling. For example, realistic diagonal cracks can be simulated only when diagonal orientated elements are present. In our study, the shear fracture plane must follow the "section" part in each single unit which has the highest stress as the "section" are the load bearing part of the cellular structure. Actually, the diagonal shear fracture plane can be also witnessed from the experimental result. A symmetric diagonal plane from top left to bottom right direction can be observed in the experiment. However, since the top and the bottom surface of the experimental sample are not perfectly flat, the shear plane is not exactly diagonal direction but somewhat deflected. Eventually, cracks generally propagated through the entire structure leading to the failure of the compressed specimen. Correspondingly, from stress-strain

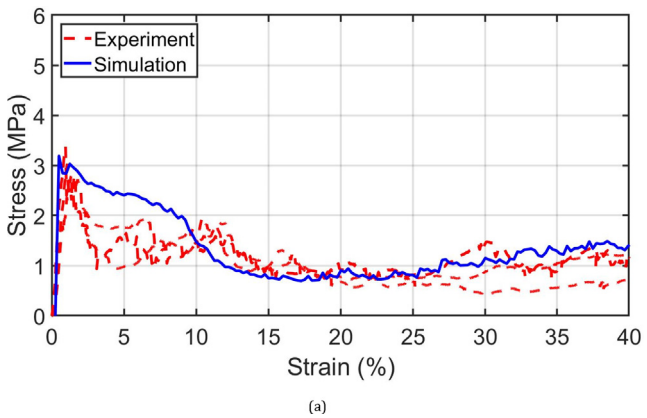

(a)

Fig. 7. Experiment and numerical simulation of P0, a) stress–strain curves, b) compression process, cracks is indicated by plastic strain.

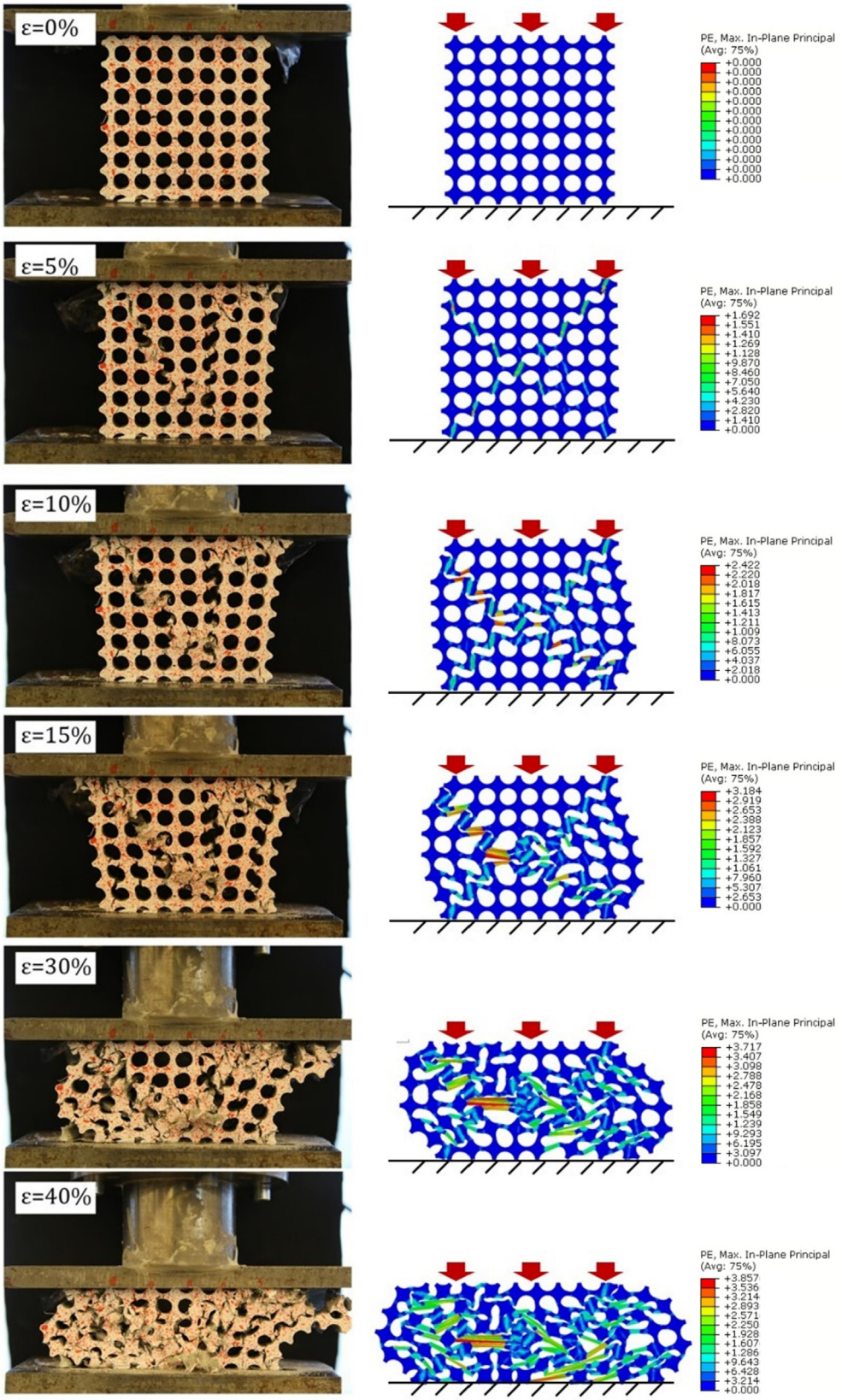

(b)

Fig. 7 (*continued*)

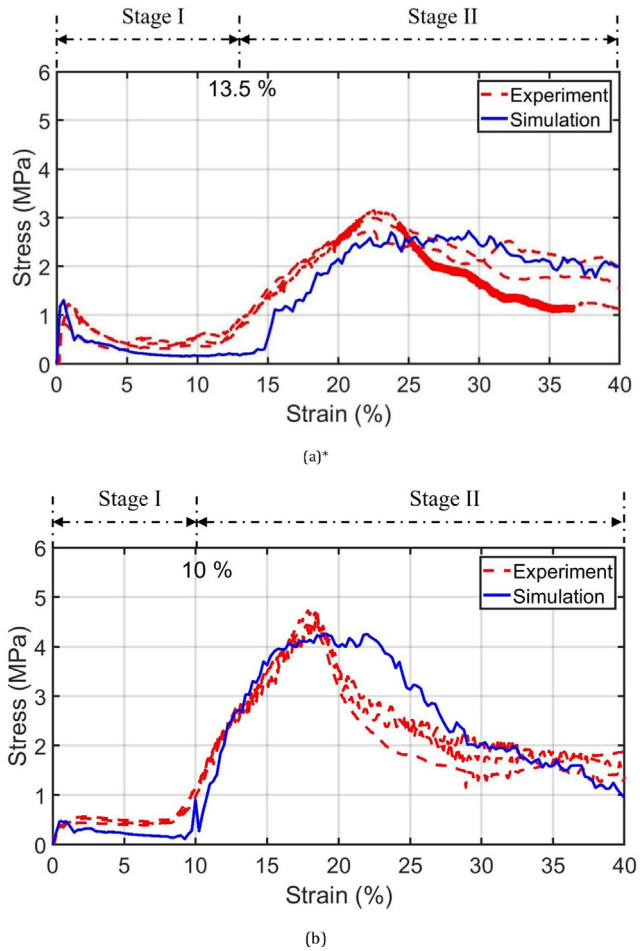

Fig. 8. Comparison of stress–strain curves obtained from experiment and simulation of a) P25 and b) P50, *experimental curves of P25 are adopted from [27].

curves (Fig. 7a), a long descending branch can be witnessed in the post peak regime. Within the entire compression process P0 did not show auxetic behavior, which is rather different from the behavior of similar P0 structure made using highly elastic polymers [53]. The Poisson's ratio development of P0 can be seen later from Fig. 10.

The compressive behavior of P25 and P50 is significantly different: obvious lateral contraction can be witnessed when P25 (see Fig. 9a) and P50 (see Fig. 9b) was compressed. Namely, the NPR or the so-called auxetic behavior was achieved. Therefore, P25 and P50 can be categorized as ACCCs (auxetic CCCs). As previously defined in [27,28], the experimental compression process of these ACCCs can be divided into two stages until 40% of strain (marked in Fig. 8). In the first stage, both from experiment and the simulated curves, the stress–strain response of the ACCCs looks quite similar to that of P0: a peak load can be found which consisted by an ascending branch and a long descending branch. The compression process of the ACCCs, however, is rather different. As can be seen from Fig. 9, the ACCCs exhibit obvious lateral contraction during the entire first stage, the cellular structure of the ACCCs was generally damaged and eventually disappeared until the ACCCs were compacted to be "solid" material. Even more detailed information can be found from the Poisson ratio curves in Fig. 10. For all three cellular structures, the experimental measured Poisson's ratio shows good consistence with the simulated results: during the entire compression process P0 shows lateral expansion, a positive Poisson's ratio was obtained as a result. Comparatively P25 and P50 show lateral contraction as soon as the compression initiated. For the ACCCs, the division of compression stages is based on their stress–strain response as well as the corresponding development of the Poisson's ratio. Throughout the first stage, the Poisson's ratio kept decreasing until a minimum Poisson's was reached at a certain strain indicating that the cellular structure was completely compacted. The first stage ended at this strain, afterwards the ACCCs started to expand under compression although the calculated Poisson's ratio is still negative.

In the first stage, the differences found between P0, P25 and P50 can be attributed to their geometrical features. The peak load values of P0, P25 and P50 is normalized by their relative density, both in the experiments and the simulations the first peak (see Fig. 11a) of P0 is always the highest and P25 is lower while the P50 is the lowest because of the stress concentration induced by the cellular structure under compression. More in-depth discussion related to the stress concentration induced by geometrical features is presented later. On the other hand, as the sections start to get in contact near the minor axis end of the ellipse and the ellipse minor axis of P25 (6 mm) was higher than P50 (4 mm), P25 had more space in each unit cell to be compressed during the first stage. Therefore, the first stage of P25 ended at 13.5% of strain while P50 ended at 10%.

Normally, elastic response of the auxetic Normalized E-modulus of the CCCs is shown in Fig. 11c, obviously the cellular structure drastically decreased E-modulus of all the CCCs comparing to the used constituent material (8.23 GPa) which can be explained by the fact that CCCs have a significantly lower density. However, for the CCCs as the relative density increases (from P0 to P50), the elastic modulus, on the contrary, decreases. This indicates that the deformation pattern or the shape of the cellular structure, and not the density, dominates the elastic response of the CCCs.

While the first stage indicated the damage and compacting process of the cellular structure, the second stage indicated the damage process of the constituent material. In the second stage, the "sections" of each unit cell started to contact and cracks started to propagate in the sections generally leading to the failure of the compacted "solid" constituent material. Accordingly, in the stress–strain curves, a second peak which consisted of another ascending and descending branch can be identified. In this sense, this process is also rather similar to a compressive damage process of conventional fiber reinforced materials. It can be seen from Fig. 11b, because of higher specimen volume, P50 (79.75 cm^3) has a higher second peak than P25 (67.68 cm^3). Meanwhile the simulated second peak load is slightly lower than the experiment which may be caused by the slight inconsistence in cellular geometry and the boundary friction between the numerical models and the real experiments. This two-stage compressive behavior was also observed in many other auxetic materials [9].

4.2. Mechanism of auxetic behavior

With regard to the auxetic mechanism, a rod-spring model was proposed in [16] for a similar centrosymmetric chiral structure however constituted by elastomers in which localized deformation is a crucial factor for the auxetic behavior. For cementitious materials, because of their low deformability, the auxetic behavior is more related to cracking rather than only elastic deformation. Regarding to the auxetic mechanism of the ACCCs in this study, more specifically, a hypothesis was raised by [27]. There, the origin of this behavior was assumed to be both the crack bridging ability due to the fibers in the constituent material and the chirality of the cellular structure. In this study, because a same mixture as in [27] was used, the influence of constituent material was eliminated. With the aid of numerical simulations, more proofs can be identified supporting the hypothesis raised in [27].

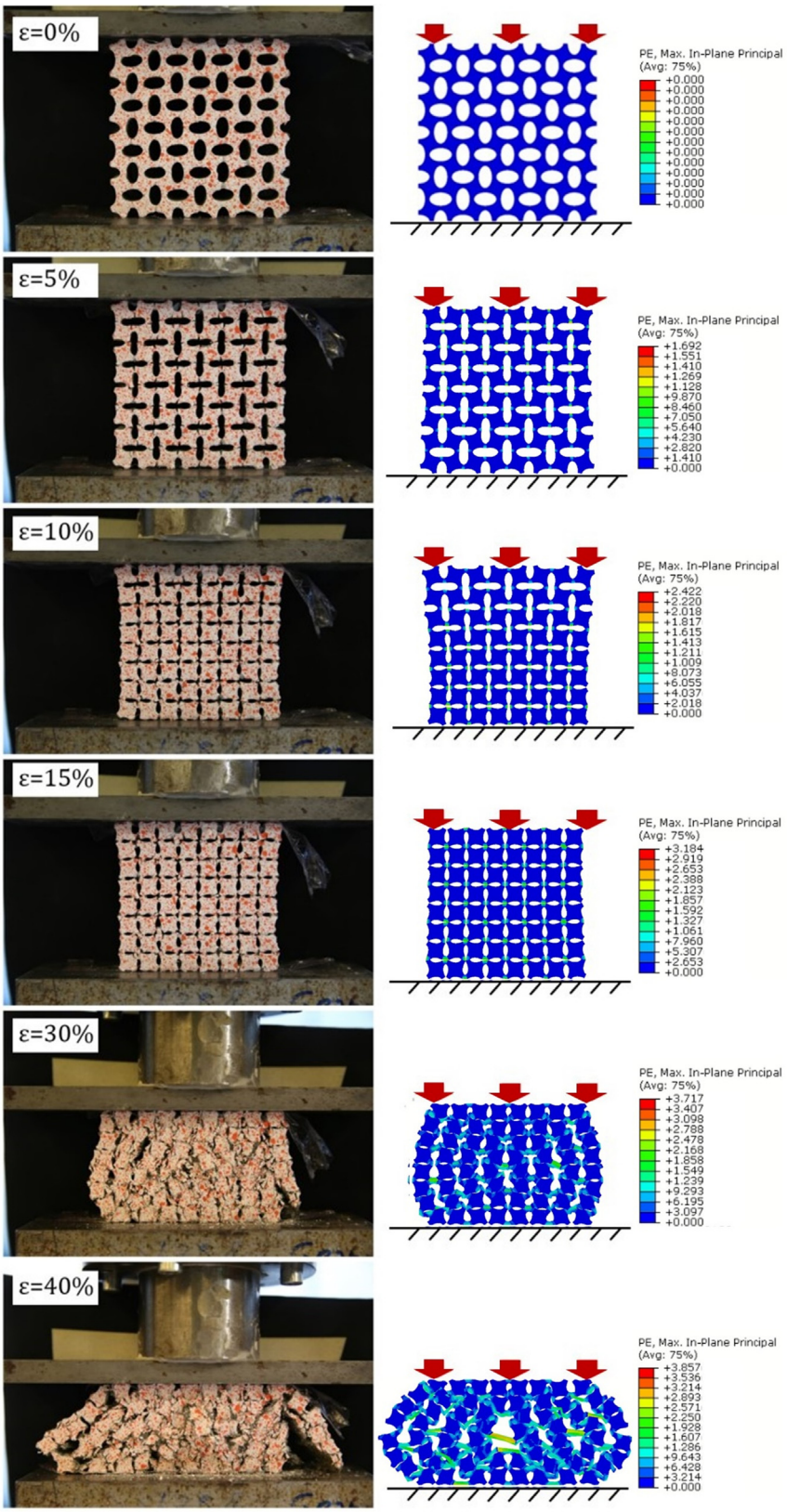

(a)*

Fig. 9. Experiment and numerical simulated compression process of a) P25 and b) P50, *several experimental compression pictures of P25 are adopted from [27].

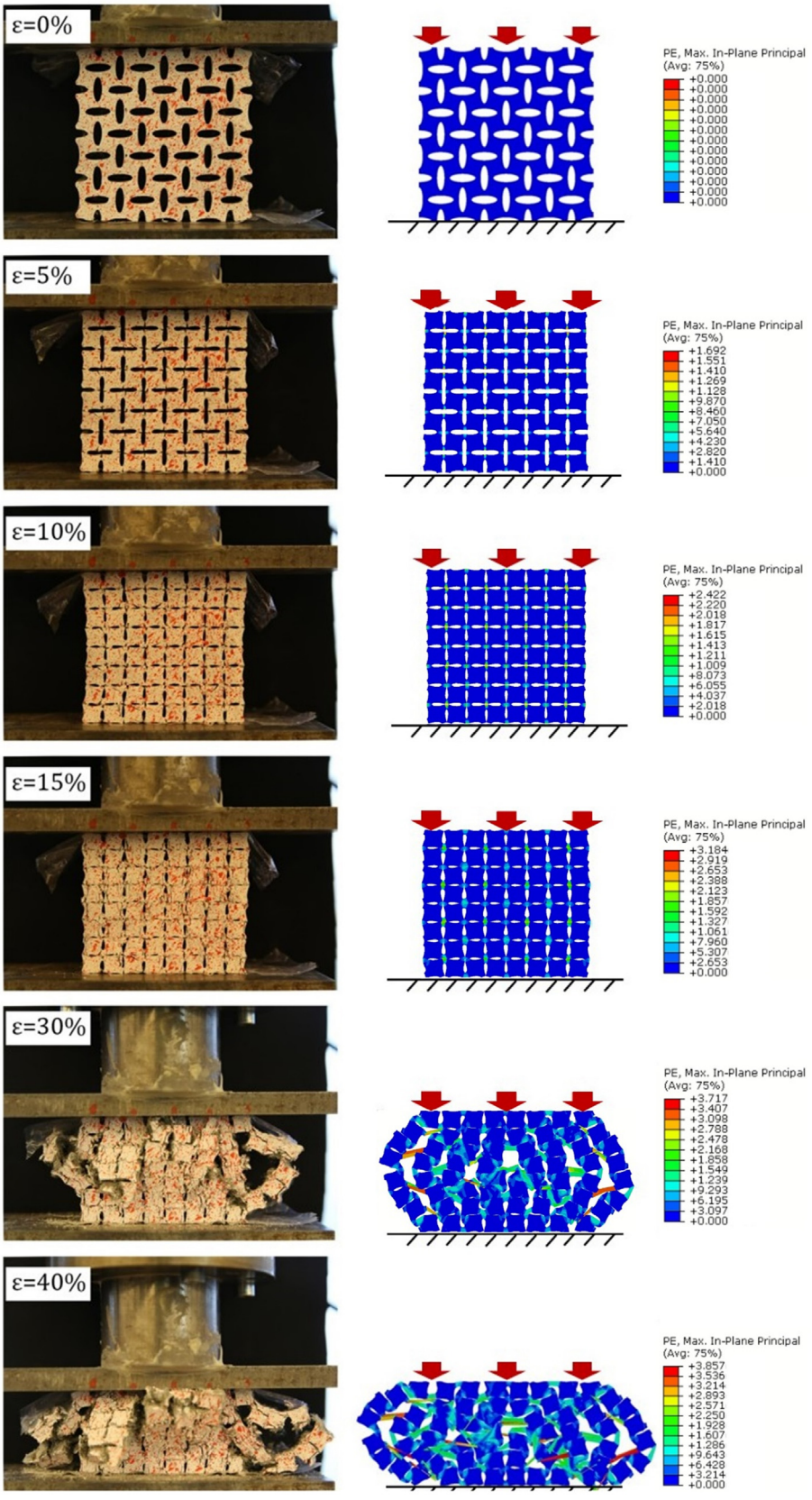

(b)

Fig. 9 (*continued*)

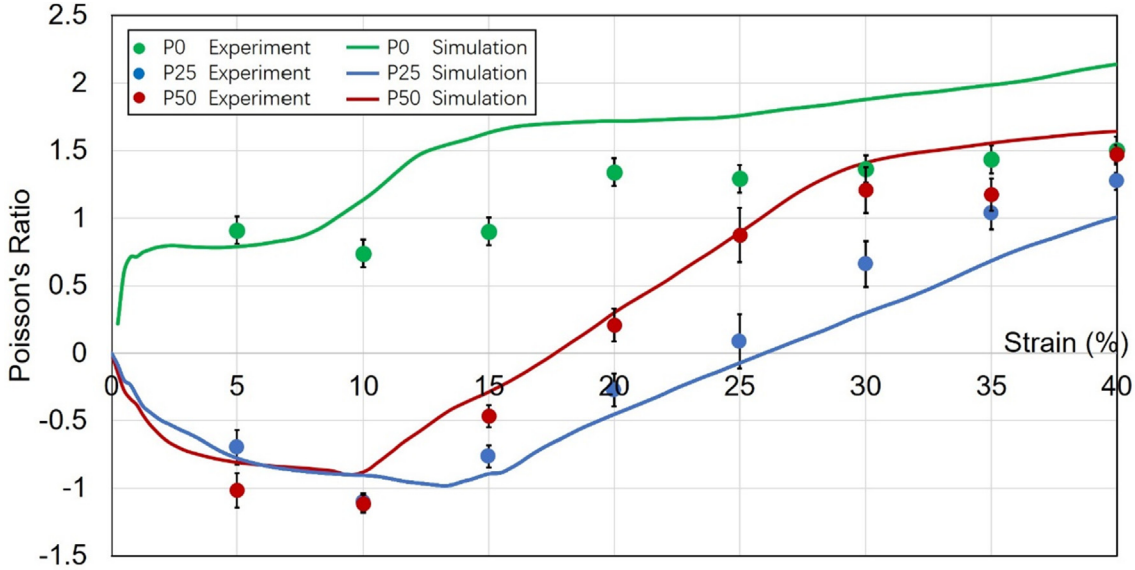

Fig. 10. Poisson's ratio of P0, P25 and P50 obtained from experiment and simulation, standard deviation is indicated; the experimental result of P25 is adopted from [27].

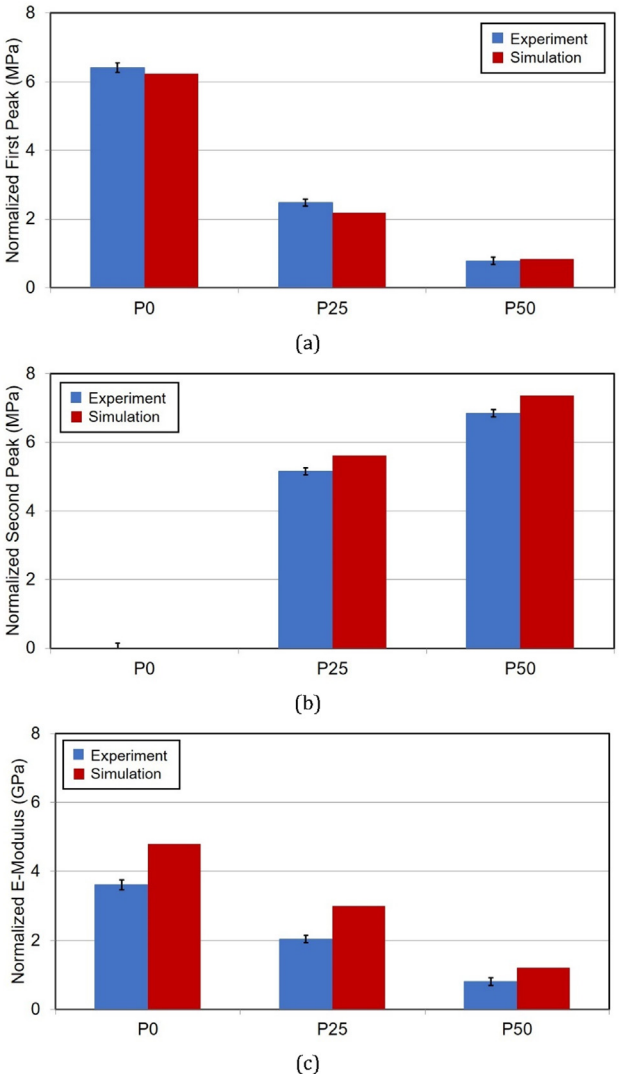

Fig. 11. Comparison of the a) the normalized first peak load, b) the normalized second peak load and c) normalized E-modulus between experiment and simulation, experiment standard deviation is indicated.

According to [27], chirality of the "sections" in each unit cell introduces stress concentration when external compressive load is applied. Fig. 12 shows the distribution of maximum principle stress (tensile stress) and minimum principal stress (compressive stress) on three cellular structures in the elastic regime subjected to the same load (250 N). It can be seen from Fig. 12a, for P0 the highest tensile stress distributes in the "section" region of the cellular structure which will eventually result in cracking when the principal tensile stress reaches the tensile strength of the constituent material. However, for P25 and P50, the tensile principal stress concentrates in the "joint" region of each unit cell. More importantly, as assumed by [27,30], when this cellular structure is loaded, because of the section chirality, the "joint" of each unit cell is submitted to a condition similar to four point bending scheme (shown in Fig. 13), under which the minor and major axis side of the ellipse is in tension and compression, respectively. The simulation results are in good agreement with this assumption: it can be seen from Fig. 12b and Fig. 12c that for both P25 and P50 tensile principal stress mainly concentrates at the "joint" near the minor axis side, meanwhile compressive stress mainly concentrates near the major axis side. Owing to the stress concentration, a crack initiates at the tension stress concentrated area as soon as the tensile stress reaches the material tensile strength. Comparing to P25, higher concentrated tensile stress can be found in P50 under the same external load (250 N): the highest tensile stress of P50 at the "joint" is almost exceeding the tensile strength (1.74 MPa) of the constituent material, while the highest tensile stress of P25 is lower than 1 MPa. This explains the fact that the first peak load of P50 is lower than P25 (see Fig. 11a).

As described in section 4.1, the cellular structure of the ACCCs was destroyed in the first stage. This process was initiated by cracking which subsequently led to compacting of the unit cell until the cellular structure generally disappeared. Auxetic behavior was observed during this process. For P25 (Fig. 14a) and P50 (Fig. 14b), cracks first appear at the tensile stress concentrated area. The simulation results and DIC results (see Fig. 15) show good agreement with regard to the cracking location. After cracking, similar to the rod-spring model described by [30], in each unit cell the joints act as hinges which allows the sections to rotate and eventually the sections get in contact with each other. As the horizontal length of the unit cell decreases with rotation, globally the CCCs exhibit auxetic behavior. In this sense, the behavior can be

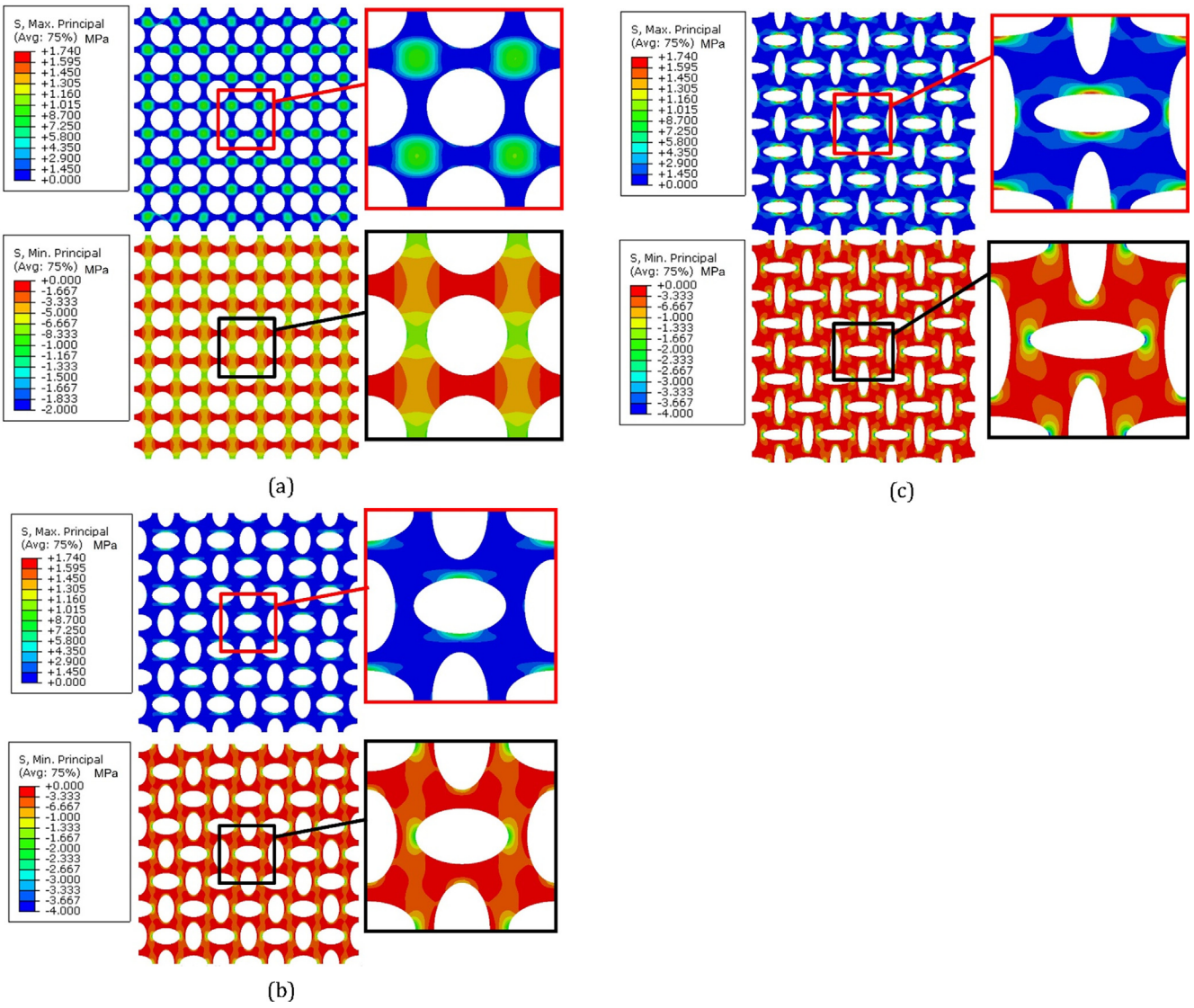

Fig. 12. Maximum and minimum principal stress distribution of a) P0, b) P25 and c) P50, note that the scale of P0 is different from P25 and P50.

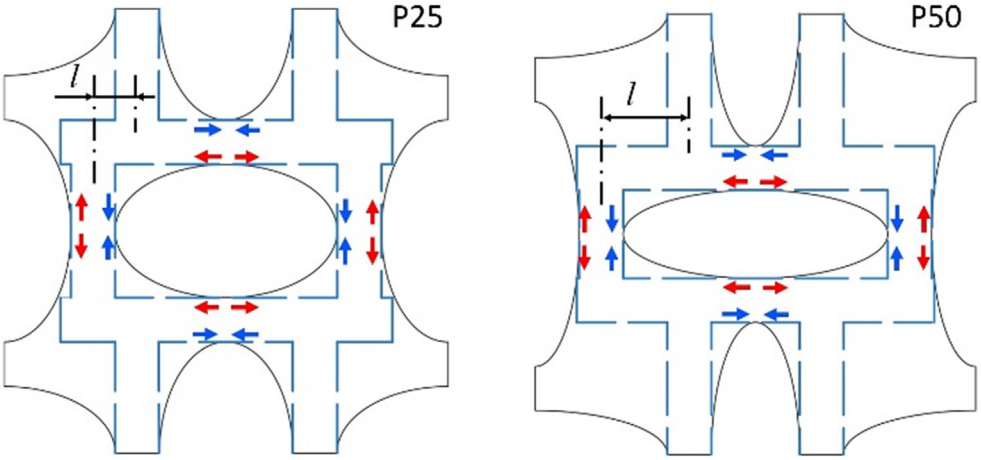

Fig. 13. Simplified loading scheme of the auxetic CCCs (P25 and P50), blue arrow and red arrow represent compressive and tensile stress respectively. (For interpretation of the references to colour in this figure legend, the reader is referred to the web version of this article.)

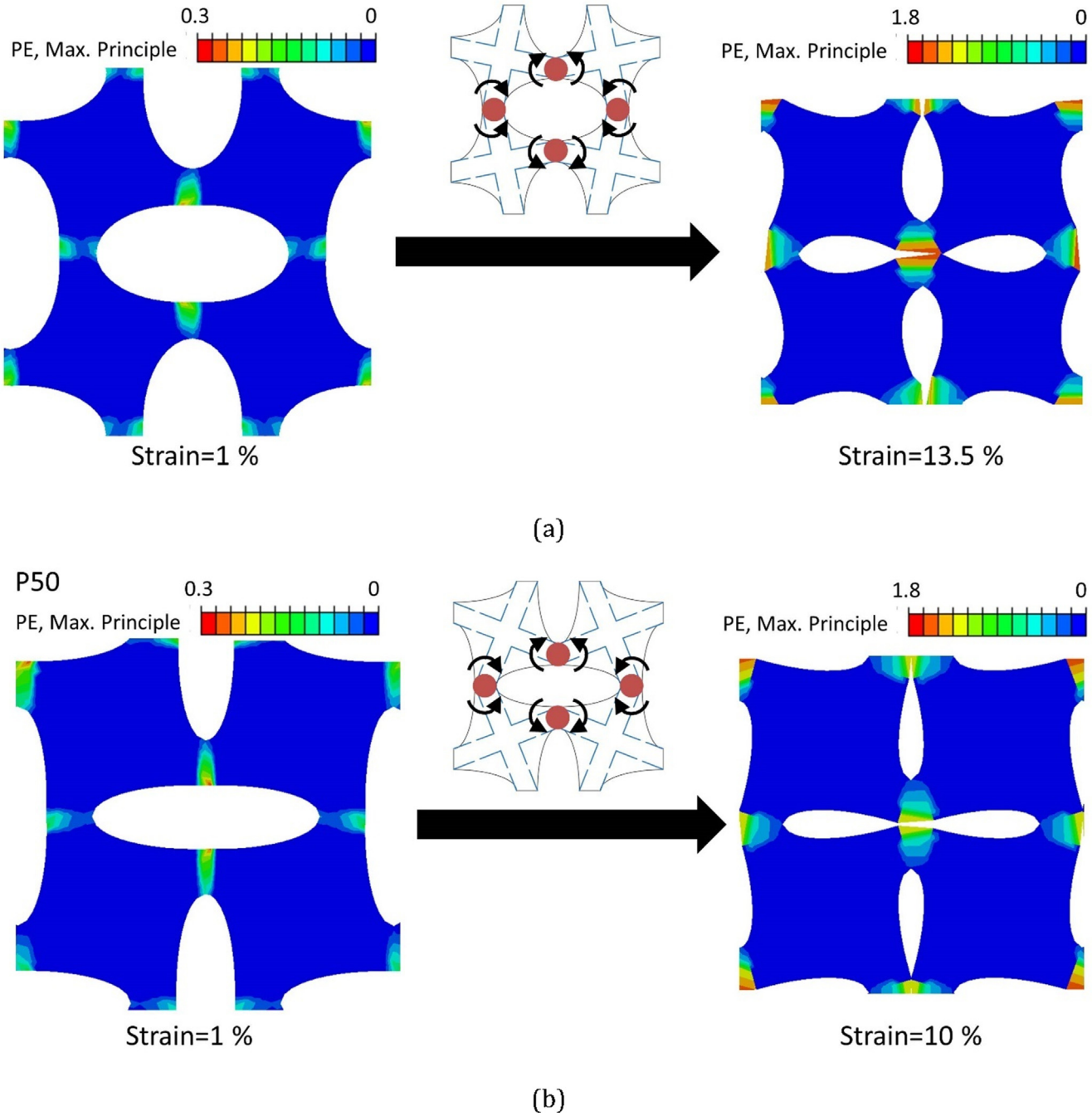

Fig. 14. Simulated compacting process of a) P25 and b) P50 unit cell by section rotation after cracking, crack is indicated by plastic deformation, plastic strain is indicated.

seen as similar to the rotating square geometries [54–56] where the joints act as nodes and the sections act as rotating bodies. In addition, because the ellipse minor axis length of P25 (6 mm, see Table 1) is 30% higher than P50 (4 mm, see Table 1), larger strain (3.5% higher than P50) is needed for P25 to be compacted. In summary, the mechanism of the auxetic behavior of ACCCs can be described as cracking initiated section rotation.

4.3. Influence of boundary conditions

Boundary restraint conditions have a significant influence on the cracking behavior of cementitious materials under uniaxial compression as the confinement provided by the loading plates affects the development of the fracture localization [32]. For bulk cementitious materials, due to the positive Poisson's ratio, uniaxial vertically compressed specimen exhibits horizontal expansion. Under high friction boundary condition, horizontal expansion near the loading plate is restrained which creates local confinement: consequently, cracking will occur in the unconfined area. A cone shape can be observed (schematics is shown in Fig. 16), with triaxial compressive stress arising locally within the specimen which leads to a higher overall peak load [32,33]. This phenomenon is comparable with the triaxial compressed concrete. For the auxetic CCCs, the confined zone can be also witnessed: however, unlike bulk cementitious materials, the compressed specimen tries to contract laterally under compressive vertical load, owing to the NPR effect. Therefore, the direction of confinement is inverted, which leads to re-entrant angle shape confined zone instead of a

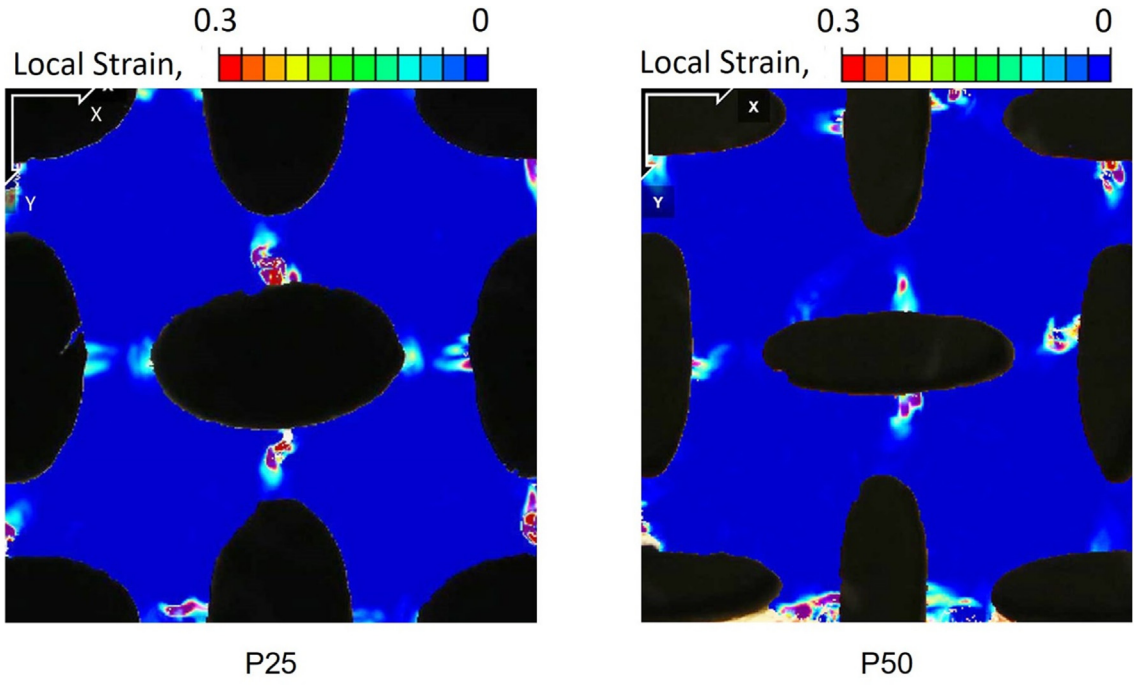

Fig. 15. DIC results on a unit cell of P25 and P50 at 1% of total strain, high local strain location indicates cracking.

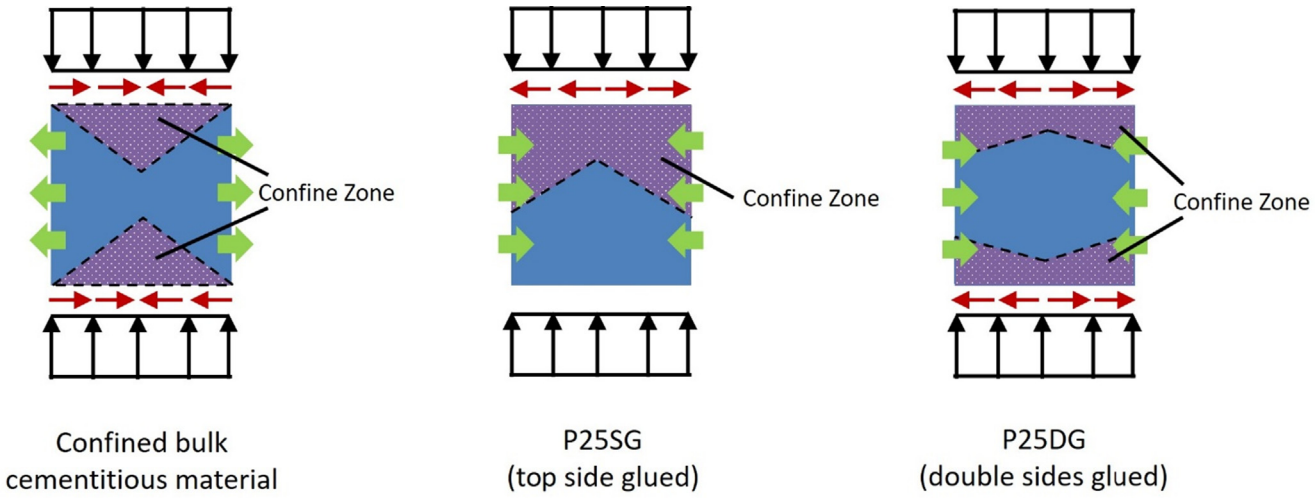

Fig. 16. Schematics of the confine zone of confined bulk cementitious material and ACCCs with top side confined (P25SG) and double side confined (P25DG).

cone. As can be seen from Fig. 17a, for P25SG (the P25 specimen with top side glued on the loading plate) at 5% strain obvious difference can be seen between the glued side (top) and low friction side (bottom). The undeformed cells show a re-entrant shape confined zone. At the low friction side (bottom), the cellular structure is compacted by a previously described cracking initiated rotation mechanism, while at the glued side (top), the cells are barely deformed because of the lateral confinement from the upper loading plate. Similarly, for P25DG (the P25 specimen with both top and bottom side glued on the loading plates) at 5% strain, both sides show re-entrant confined zones consisting of undeformed cells near the two loading plates (see Fig. 17b), similar deformation pattern can be also seen on elastomers[46], however in elastic stage caused by elastic instability.

The stress–strain response of P25DG and P25SG is also obviously affected by the boundary restraint. As already discussed in the previous section that void closure causes the typical two-stage stress–strain response of P25. Under low friction condition, the cells are not confined and are free to crack and deform. Consequently, the first peak from the P25 stress–strain curve depicts cracking of the cellular structure, while subsequently the second load increase after section rotation depicts compacting of the constituent material. Under glued boundary conditions, the typical second load increase still can be found both from the experiment and simulated stress–strain curves (see Fig. 18). However, the crack initiation as well as the section rotation were restrained. As shown in Fig. 19, due to the highest applied restraint, the normalized first peak load of P25DG (3.48 MPa from the experiment and 3.18 MPa from the simulation) is also the highest. The first peak load of P25SG is lower (2.75 MPa from the experiment and 2.56 MPa from the simulation) because of less restraint. Finally, the first peak load of P25 is the lowest (2.18 MPa from experiment

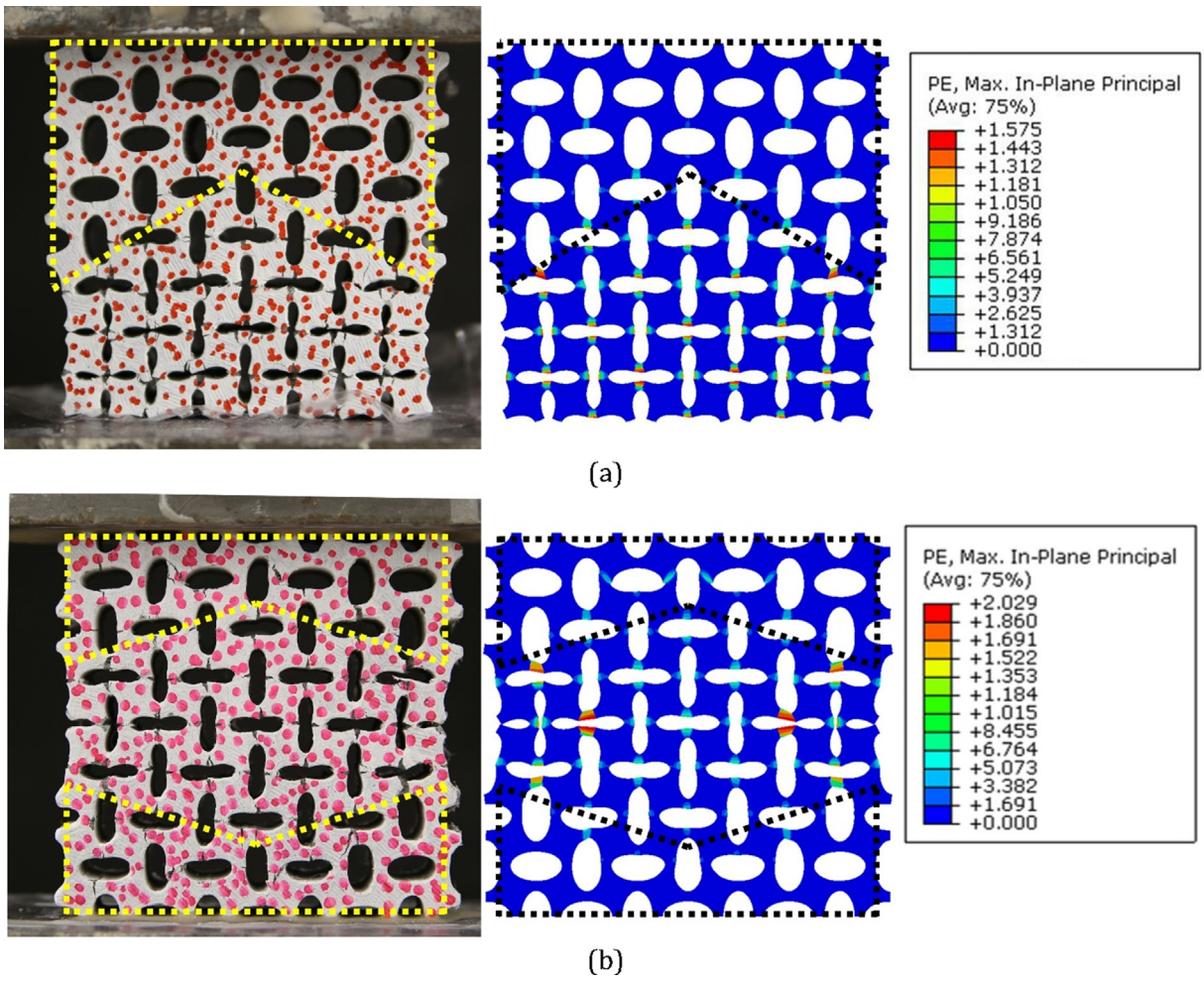

Fig. 17. Deformed specimen of a) P25SG and b) P25DG at 5% strain from the experiment and the simulation, confined zones are marked by dashed lines.

and 2.47 MPa from simulation) because of the low friction boundary condition. This phenomenon can be attributed to the confined fracture localization which is similar to the fact that bulk cementitious materials show higher compressive strength under restraint boundary condition [32]. As mentioned previously, cementitious materials are very heterogenous, their compressive failure is a process of tensile microcracking (Mode I fracture at microscale) and crack localization (crack shearing). For bulk cementitious materials, compressive strength is reached around the onset of crack localization. When a macroscopic compressive load is present and the specimen is laterally confinement, lateral tensile stresses introduced at the micro heterogeneities are reduced by the confinement. Higher compressive load is then required to generate microcracks as a result. Also, when microcracks are present, lower shear stress will be present due to lateral confinement which slows down shearing of the microcracks due to an increase of the frictional stresses on the crack surface and compressive strength is increased as a result. For P25, the first peak strength is mainly determined by the tensile cracking at the joints. Higher compressive load is required to generate microcracks at the joints due to lateral confinement, as a result first peak strength of confined P25 is higher. After the first peak, the second load increase of P25DG and P25SG is still visible both in experiment and simulated curves. However, as the cell sections rotation near the loading plates was restrained, less cells can deform and be compacted which led to slower load increase and is seen in the stress–strain curves by much longer and milder ascending branch under glued boundary conditions.

5. Potential application of the CCCs

As a cellular material, low unit weight is an important feature of the CCCs. In our study, the density of the CCCs are 928 kg/m^3 (P0), 987 kg/m^3 (P25) and 1163 kg/m^3 (P50) respectively, which are considerably lower than bulk cementitious materials (1870 kg/m^3 for the mix we used). In this aspect, the CCCs are rather similar to a widely used lightweight civil engineering material: foam concrete. Regarding the compressive strength, the CCCs are rather comparable to the foam concrete with a density from 900 kg/m^3 to 1200 kg/m^3, see Fig. 20. On the other hand, as shown in Fig. 21, the compressibility (defined as the strain at compressive strength by percentage) of the ACCCs (22.4% for P25 and 18.0% for P50) is distinctively higher than normal foam concrete (around 1.0%). The large compressibility of ACCCs ensures their excellent energy dissipation capacity (shown in Fig. 22, defined as the area under load–displacement curves divided by volume, due to the compressed displacement varies in different existing researches [57–62], the energy dissipation properties of foam concrete has rather large deviation). Comparing to energy dissipation property of foam concrete (0.01 J/cm^3 to 1.70 J/cm^3 with an average value of 0.70 J/cm^3), the energy dissipation properties of the ACCCs is good enough to be applied as supplement or substitute. In addition, in the construction of roads or bridge embankments, foam concrete (density from 350 kg/m^3 to 1000 kg/m^3, compressive strength from 0.5 MPa to 3.5 MPa[63,64]) has been used as filler of the embankment under the road pavement to control settlements of the underlying soil foundation. Using as filler for embank-

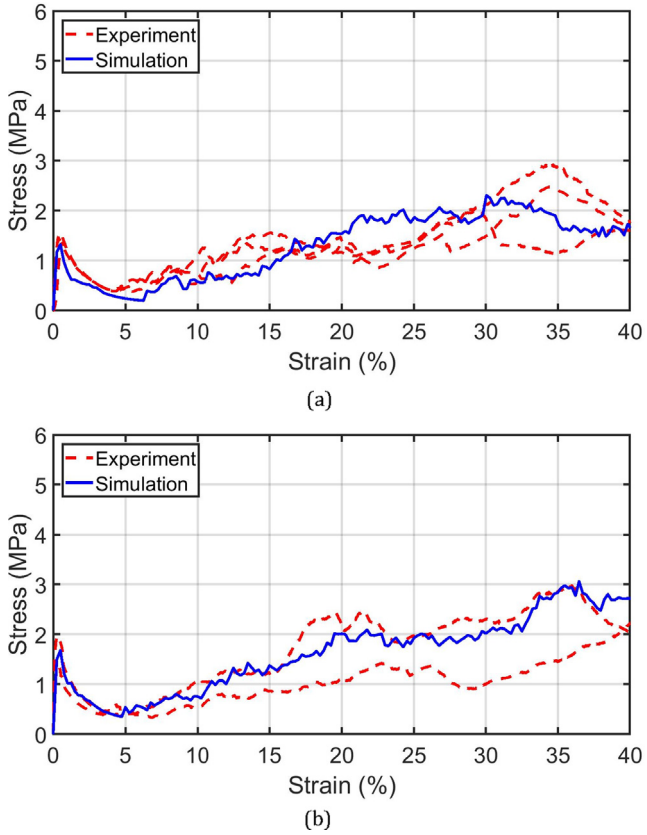

Fig. 18. Stress–strain curves of a) P25SG and b) P25DG obtained from experiment and simulation.

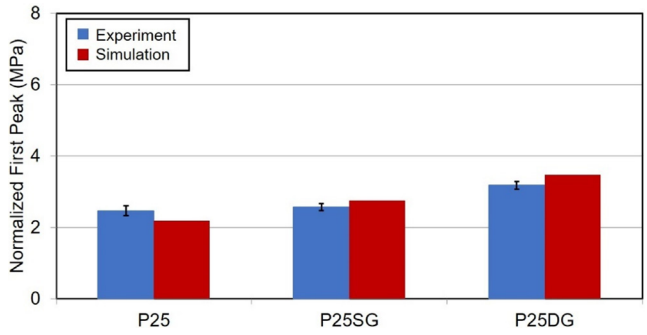

Fig. 19. Comparison of the normalized first peak load of the ACCCs under different boundary conditions.

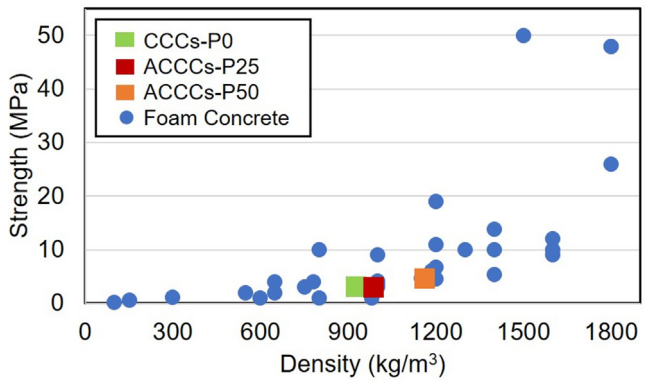

Fig. 20. Compressive strength comparison of the CCCs and foam concrete, data of the foam concrete is adopted from [65,66].

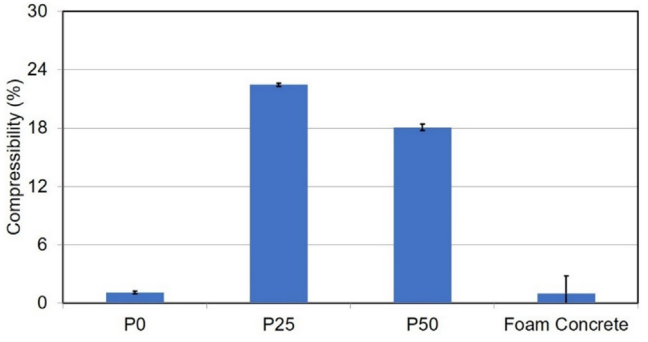

Fig. 21. Compressibility of the CCCs and foam concrete, standard deviation is indicated; data of the foam concrete is adopted from [59–62,67]

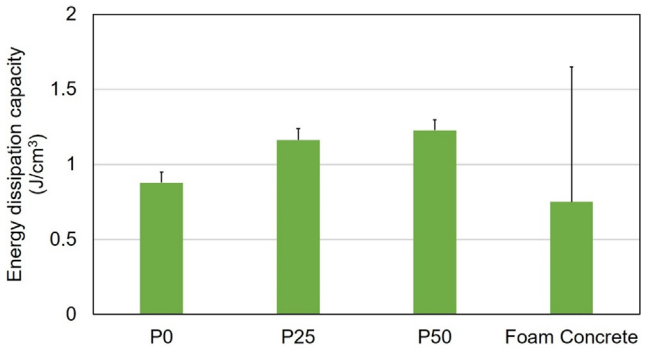

Fig. 22. Energy dissipation capacity of the CCCs; data of the foam concrete is adopted from [59–62,67], due to the compressed strain varies in these studies [59–62,67], large deviation of foam concrete can be witnessed.

ment could be a potential application for the ACCCs, not only for their low density and strength (which are similar to those of foam concrete), but, more importantly, the negative Poisson's ratio. The ACCCs do not laterally expand when loaded, thereby avoiding added pressure on adjacent structures which is an excellent feature especially when existing embankment need to be widened.

6. Conclusions

In the present work, a study coupling experiments and numerical simulations was performed to investigate the compressive behavior of cementitious cellular composites (CCCs) with negative Poisson's ration (NPR). Based on the obtained experimental and numerical results and corresponding analysis, the main conclusions can be drawn as follows:

- Concrete damage plasticity model (CDPM) proves to be an adequate tool to simulate the uniaxial compressive behavior of this type of cementitious cellular composites (CCCs) regarding to their deformation pattern, Poisson's ratio and stress–strain response.
- Compressive deformation patterns of the CCCs is crucially influenced by the geometrical features. Only CCCs with chiral sections (P25 and P50) show negative Poisson's ratio and can be defined as auxetic CCCs (ACCCs).
- Physical and mechanical properties of the ACCCs can be tuned and modified by varying the pattern deformation factor. Increasing the pattern deformation factor increases the relative density compressive strength while decreasing the E-modulus.
- A cracking initiated section rotation mechanism is identified as a source of the ACCCs auxetic behavior, in contrast to the elastic instability mechanism of the elastomers with similar cellular structures.

- Under boundary confinement, compressed ACCCs undergo lateral restraint. Different from the commonly found cone shape fracture zone contrary to that of bulk cementitious materials which leads to a re-entrant shape fracture zone.
- The ACCCs have similar physical and mechanical properties to foam concrete used in engineering practice, while their deformability is significantly higher. This makes ACCCs a potential supplement or an alternative of foam concrete in applications such as energy absorption and settlement mitigation.

According to the obtained results, the properties of the CCCs are tunable and can be improved by modifying the cellular structure. Meanwhile, combing the modification of cellular structure and tailoring the properties of the constituent materials may also improve mechanical performance of the CCCs and this can be a future research direction.

CRediT authorship contribution statement

Yading Xu: Investigation, Writing - original draft. **Erik Schlangen:** Writing - review & editing. **Mladena Luković:** Writing - review & editing. **Branko Šavija:** Investigation, Writing - review & editing.

Declaration of Competing Interest

The authors declare that they have no known competing financial interests or personal relationships that could have appeared to influence the work reported in this paper.

Acknowledgements

Yading Xu would like to acknowledge the funding supported by China Scholarship Council (CSC) under the grant No. 201708110187. The authors would like to acknowledge Mr. Jorick Wolbert for his support in the specimen preparation and mechanical tests.

References

[1] K.E. Evans, M.A. Nkansah, I.J. Hutchinson, S.C. Rogers, Molecular network design, Nature 353 (6340) (1991) 124.
[2] R. Critchley et al., A review of the manufacture, mechanical properties and potential applications of auxetic foams, Physica Status Solidi (b) 250 (10) (2013) 1963–1982.
[3] Y. Prawoto, Seeing auxetic materials from the mechanics point of view: a structural review on the negative Poisson's ratio, Comput. Mater. Sci. 58 (2012) 140–153.
[4] X. Ren, Studies on three-dimensional metamaterials and tubular structures with negative Poisson's ratio, RMIT University, Australia, 2017.
[5] T.F. Zhao et al., Thickness effect on mechanical behavior of auxetic sintered metal fiber sheets, Mater. Des. 167 (2019) 107635.
[6] Y. Yao et al., A novel auxetic structure based bone screw design: Tensile mechanical characterization and pullout fixation strength evaluation, Mater. Des. 188 (2020) 108424.
[7] J.S. Hu, B.L. Wang, J.E. Li, K.F. Wang, Thermal shock resistance behavior of auxetic ceramic honeycombs with a central crack or an edge crack, Ceram. Int. 46(8, Part B) (2020) 11835-11845.
[8] C.L. Willey, P.R. Buskohl, A.T. Juhl, Electronically tunable auxetic behavior of shunted piezoelectric elements, J. Mech. Phys. Solids 103873 (2020).
[9] M. Taylor, et al. "A novel auxetic structure with enhanced impact performance by means of periodic tessellation with variable Poisson's ratio." Dyn. Behav. Mater., Volume 1. Springer, Cham, 201211-218.
[10] J. Shen et al., Simple cubic three-dimensional auxetic metamaterials, Physica Status Solidi (b) 251 (8) (2014) 1515–1522.
[11] A. Bezazi, F. Scarpa, Tensile fatigue of conventional and negative Poisson's ratio open cell PU foams, Int. J. Fatigue 31 (3) (2009) 488–494.
[12] M.J. Mirzaali et al., Multi-material 3D printed mechanical metamaterials: Rational design of elastic properties through spatial distribution of hard and soft phases, Appl. Phys. Lett. 113 (24) (2018) 241903.
[13] M.J. Mirzaali et al., Rational design of soft mechanical metamaterials: Independent tailoring of elastic properties with randomness, Appl. Phys. Lett. 111 (5) (2017) 051903.
[14] Y. Xue, W. Wang, F. Han, Enhanced compressive mechanical properties of aluminum based auxetic lattice structures filled with polymers, Compos. B Eng. 171 (2019) 183–191.
[15] K.K. Dudek, R. Gatt, J.N. Grima, 3D composite metamaterial with magnetic inclusions exhibiting negative stiffness and auxetic behaviour, Mater. Des. 187 (2020) 108403.
[16] Mir, Mariam, et al. "Review of mechanics and applications of auxetic structures." Adv. Mater. Sci. Eng., vol. 2014, Article ID 753496, 17 pages, 2014.
[17] H.L. Tan et al., In-plane crashworthiness of re-entrant hierarchical honeycombs with negative Poisson's ratio, Compos. Struct. 229 (2019) 111415.18.
[18] Z.D. Sha et al., Metallic glass-based chiral nanolattice: Light weight, auxeticity, and superior mechanical properties, Mater. Today 20 (10) (2017) 569–576.
[19] J. Smardzewski, Experimental and numerical analysis of wooden sandwich panels with an auxetic core and oval cells, Mater. Des. 183 (2019) 108159.
[20] C. Soyarslan, V. Blümer, S. Bargmann, Tunable auxeticity and elastomechanical symmetry in a class of very low density core-shell cubic crystals, Acta Mater. 177 (2019) 280–292.
[21] Z. Wang, A. Zulifqar, H.u. Hong, Auxetic composites in aerospace engineering, Adv. Compos. Mater. Aerosp. Eng. (2016) 213–240.
[22] Y. Guo et al., Deformation behaviors and energy absorption of auxetic lattice cylindrical structures under axial crushing load, Aerosp. Sci. Technol. 105662 (2020).
[23] M.R. Sloan, J.R. Wright, K.E. Evans, The helical auxetic yarn–a novel structure for composites and textiles; geometry, manufacture and mechanical properties, Mech. Mater. 43 (9) (2011) 476–486.
[24] F. Steffens, S. Rana, R. Fangueiro, Development of novel auxetic textile structures using high performance fibres, Mater. Des. 106 (2016) 81–89.
[25] H. Hu, M. Zhang, Y. Liu, Auxetic Textiles, Woodhead Publishing, 2019.
[26] Y. Ma et al., A nonlinear auxetic structural vibration damper with metal rubber particles, Smart Mater. Struct. 22 (8) (2013) 084012.
[27] Y. Xu et al., Cementitious cellular composites with auxetic behavior, Cem. Concr. Compos. 103624 (2020).
[28] Xu, Yading, Šavija Branko, and Schlangen Erik. "Compression Behaviors Of Cementitious Cellular Composites With Negative Poisson's Ratio." Proceedings of the 10th International Conference on Fracture Mechanics of Concrete and Concrete Structures. 2019.
[29] B. Florijn, C. Coulais, M. van Hecke, Programmable mechanical metamaterials: the role of geometry, Soft Matter 12 (42) (2016) 8736–8743.
[30] Y. Zhang, Y. Wang, C.Q. Chen, Ordered deformation localization in cellular mechanical metamaterials, J. Mech. Phys. Solids 123 (2019) 28–40.
[31] C. Coulais, Periodic cellular materials with nonlinear elastic homogenized stress-strain response at small strains, Int. J. Solids Struct. 97 (2016) 226–238.
[32] M.R.A. Van Vliet, Van Mier, Jan GM. "Experimental investigation of concrete fracture under uniaxial compression." Mechanics of Cohesive-frictional Materials: An International Journal on Experiments, Modelling and Computation of Materials and Structures 1.1 (1996): 115-127.
[33] Van Mier, G.M. Jan. Fracture processes of concrete. CRC press, 2017.
[34] Bertil Persson, Poisson's ratio of high-performance concrete, Cem. Concr. Res. 29 (10) (1999) 1647–1653.
[35] Julian Carrillo, Julieth Ramirez, Juan Lizarazo-Marriaga, Modulus of elasticity and Poisson's ratio of fiber-reinforced concrete in Colombia from ultrasonic pulse velocities, J. Build. Eng. 23 (2019) 18–26.
[36] Yue Li, Yaqiang Li, Evaluation of elastic properties of fiber reinforced concrete with homogenization theory and finite element simulation, Constr. Build. Mater. 200 (2019) 301–309.
[37] Van Zijl, P.A.G. Gideon, Dirk JA de Jager, Improved ductility of SHCC retrofitted unreinforced load bearing masonry via a strip-debonded approach, J. Build. Eng. 24 (2019) 100722.
[38] Yi Tao, Jian-Fei Chen, Concrete damage plasticity model for modeling FRP-to-concrete bond behavior, J. Compos. Constr. 19 (1) (2015) 04014026.
[39] Yin Chi et al., Finite element modeling of steel-polypropylene hybrid fiber reinforced concrete using modified concrete damaged plasticity, Eng. Struct. 148 (2017) 23–35.
[40] Dan Meng et al., Mechanical behaviour of a polyvinyl alcohol fibre reinforced engineered cementitious composite (PVA-ECC) using local ingredients, Constr. Build. Mater. 141 (2017) 259–270.
[41] Van Mier, G.M. Jan, Concrete Fracture: A Multiscale Approach, CRC Press, 2012.
[42] Mladena Luković et al., Tailoring strain-hardening cementitious composite repair systems through numerical experimentation, Cem. Concr. Compos. 53 (2014) 200–213.
[43] Li, C. Victor. "From micromechanics to structural engineering-the design of cementitous composites for civil engineering applications." 10.2 (1993): 37s-48s.
[44] Victor C. Li et al., Interface tailoring for strain-hardening polyvinyl alcohol-engineered cementitious composite (PVA-ECC), Mater. J. 99 (5) (2002) 463–472.
[45] Victor C. Li, On engineered cementitious composites (ECC), J. Adv. Concr. Technol. 1 (3) (2003) 215–230.
[46] Yading Xu, Branko Šavija, Development of strain hardening cementitious composite (SHCC) reinforced with 3D printed polymeric reinforcement: Mechanical properties, Compos. B Eng. 174 (2019) 107011.
[47] Yading Xu et al., Deformation and fracture of 3D printed disordered lattice materials: Experiments and modeling, Mater. Des. 162 (2019) 143–153.

[48] Schlangen, Erik. "Crack development in concrete, Part 1: Fracture experiments and CT-scan observations." Key Eng. Mater.. Vol. 385. Trans Tech Publications Ltd, 2008.
[49] Schlangen, Erik. "Crack development in concrete, part 2: modelling of fracture process." Key Eng. Mater. Vol. 385. Trans Tech Publications Ltd, 2008.
[50] Branko Šavija, Mladena Luković, Erik Schlangen, Lattice modeling of rapid chloride migration in concrete, Cem. Concr. Res. 61 (2014) 49–63.
[51] Doo-Yeol Yoo, Nemkumar Banthia, Mechanical properties of ultra-high-performance fiber-reinforced concrete: A review, Cem. Concr. Compos. 73 (2016) 267–280.
[52] Zdeněk P. Bažant, Yuyin Xiang, Size effect in compression fracture: splitting crack band propagation, J. Eng. Mech. 123 (2) (1997) 162–172.46.
[53] Katia Bertoldi et al., Negative Poisson's ratio behavior induced by an elastic instability, Adv. Mater. 22 (3) (2010) 361–366.
[54] Hou Xiaonan, Vadim V. Silberschmidt. "Metamaterials with negative poisson's ratio: A review of mechanical properties and deformation mechanisms." Mech. Adv. Mater. Springer, Cham, 2015. 155-179.
[55] Joseph N. Grima et al., Smart metamaterials with tunable auxetic and other properties, Smart Mater. Struct. 22 (8) (2013) 084016.
[56] Wenwang Wu et al., Mechanical design and multifunctional applications of chiral mechanical metamaterials: A review, Mater. Des. 107950 (2019).
[57] Bo Wang et al., Investigation of low-velocity impact behaviors of foamed concrete material, Compos. B Eng. 162 (2019) 491–499.
[58] Weimin Nian, Kolluru VL Subramaniam, Yiannis Andreopoulos, Experimental investigation on blast response of cellular concrete, Int. J. Impact Eng. 96 (2016) 105–115.
[59] Thang T. Nguyen et al., Experimental and numerical investigation of influence of air-voids on the compressive behaviour of foamed concrete, Mater. Des. 130 (2017) 103–119.
[60] Buyun Su et al., Experimental investigation on the mechanical behavior of foamed concrete under uniaxial and triaxial loading, Constr. Build. Mater. 209 (2019) 41–51.
[61] Thang T. Nguyen et al., A micromechanical investigation for the effects of pore size and its distribution on geopolymer foam concrete under uniaxial compression, Eng. Fract. Mech. 209 (2019) 228–244.
[62] Yuanyi Yang, Qi Zhou, Yi Deng, The reinforcement attributes of multi-scale hybrid fiber throughout the uniaxial compression of ultra-low-weight foamed cement-based composites, Constr. Build. Mater. 242 (2020) 118184.
[63] Xiaona Shi, Junjie Huang, Su. Qian, Experimental and numerical analyses of lightweight foamed concrete as filler for widening embankment, Constr. Build. Mater. 250 (2020) 118897.
[64] Jun-jie Huang et al., Experimental study on use of lightweight foam concrete as subgrade bed filler of ballastless track, Constr. Build. Mater. 149 (2017) 911–920.
[65] Lina Chica, Albert Alzate, Cellular concrete review: New trends for application in construction, Constr. Build. Mater. 200 (2019) 637–647.
[66] YH Mugahed Amran, Nima Farzadnia, A.A. Abang Ali., Properties and applications of foamed concrete; a review, Constr. Build. Mater. 101 (2015) 990–1005.
[67] E.A. Flores-Johnson, Q.M. Li, Structural behaviour of composite sandwich panels with plain and fibre-reinforced foamed concrete cores and corrugated steel faces, Compos. Struct. 94 (5) (2012) 1555–1563.